

Parametric Intrusive Reduced Order Models enhanced with Machine Learning Correction Terms

Anna Ivagnes

SISSA, International School for Advanced Studies,
Mathematics Area, mathLab, Trieste, Italy.
aivagnes@sissa.it

Giovanni Stabile

Sant'Anna School of Advanced Studies
The Biorobotics Institute, Pontedera, Pisa, Italy.
giovanni.stabile@santannapisa.it

Gianluigi Rozza

SISSA, International School for Advanced Studies,
Mathematics Area, mathLab, Trieste, Italy.
grozza@sissa.it

Abstract

*In this paper, we propose an equation-based parametric Reduced Order Model (ROM), whose accuracy is improved with data-driven terms added into the reduced equations. These additions have the aim of reintroducing contributions that in standard ROMs are not taken into account. In particular, in this work we consider two types of contributions: the **turbulence modeling**, added through a reduced-order approximation of the eddy viscosity field, and the **correction model**, aimed to re-introduce the contribution of the discarded modes. Both approaches have been investigated in previous works such as [32, 19, 22, 21] and the goal of this paper is to extend the model to a **parametric** setting making use of ad-hoc machine learning procedures. More in detail, we investigate different neural networks' architectures, from simple dense feed-forward to Long-Short Term Memory neural networks, in order to find the most suitable model for the re-introduced contributions. We tested the methods on two test cases with different behaviors: the periodic turbulent flow past a circular cylinder and the unsteady turbulent flow in a channel-driven cavity. In both cases, the parameter considered is the Reynolds number and the machine learning-enhanced ROM considerably improved the pressure and velocity accuracy with respect to the standard ROM. A visual version of the abstract can be found in Figure 1.*

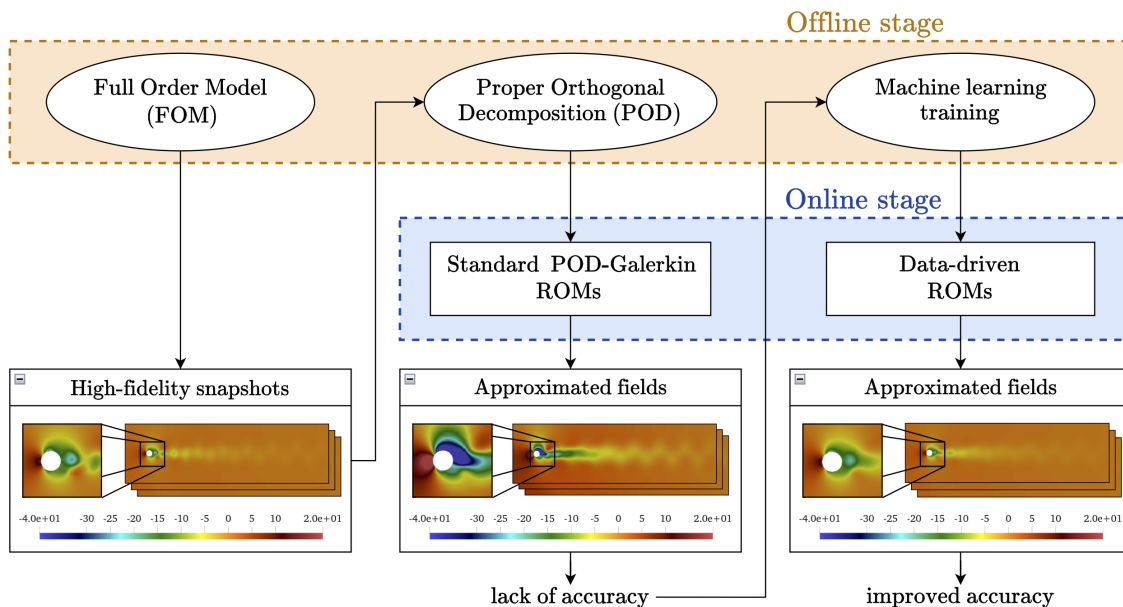


Figure 1: Visual abstract.

1. INTRODUCTION

Reduced Order Models (ROMs) [9, 10, 11, 43, 42, 44] are a powerful tool used to reduce the computational effort of time-demanding simulations. One of the fields where this class of techniques is widespread is Computational Fluid Dynamics, where high-fidelity simulations may take days or weeks, even in the case of parallel computations on many cores. For this reason, a simplified model is necessary to efficiently compute the solutions for unseen configurations.

Most of the ROMs are built upon an *offline-online* paradigm [44]. The *offline* stage consists of the computation of a large number of expensive high-fidelity simulations, performed after setting the Full Order Model (FOM), which is usually a discretized version of complex PDEs, like the Navier–Stokes Equations (NSE). The goal of this stage is the collection of the so-called *snapshots*, namely the solutions of the simulations. On the other hand, in the *online* stage the full-order manifold is projected into a space with reduced dimensionality, resulting in a reduced representation of the snapshots. This reduction step may be assessed both with linear or nonlinear approaches. In particular, we employ the Proper Orthogonal Decomposition (POD) [25, 13], a linear technique which may be considered equivalent to the Principal Component Analysis (PCA) [38, 55] and Singular Value Decomposition (SVD) [27, 17, 16].

While the offline stage usually employs the numerical resolution of complex PDEs, in *intrusive* ROMs the online stage allows for the resolution of ODEs, which consists of a reduced and simplified version of the FOM.

In particular, in this contribution, we focus on POD-Galerkin ROMs, that are based on a Galerkin projection [35, 12, 26, 7]. The main assumption of these models is that the solution may be approximated as a convex combination of a reduced number of global basis (the *modes*), whose

coefficients are the reduced representations, namely the unknown variables in the ROM. The above-mentioned linearity assumption may make the model inaccurate in the case of advection-dominated flows and where transport phenomena are dominant.

In the POD framework, the choice of the latent dimension is influenced by the singular values' decay and it has to be done *a priori*.

The goal of the ROM community is usually to retain a small number of modes, and to have efficient online simulations, namely a *marginally-resolved* regime. In this regime, the number of modes is enough to capture the dynamics of the system, but the POD-Galerkin ROM may lead to inaccurate results [41, 20].

Indeed, in advection-dominated cases, where the decay is slow, POD-Galerkin ROMs may require hundreds of modes to provide accurate results.

The inaccuracy may be caused by the formation of spurious oscillations in the approximated solution or by the ill-conditioning of the reduced system. This motivates the use of data-driven techniques to stabilize and/or enhance the system solution. Some examples of works integrating ROMs with machine learning strategies are [58, 37, 39, 23].

More in detail, a widespread class of stabilization approaches is the regularized ROM, which aims to smooth out the noisy and inaccurate solution acting as a *filter*. Some examples are the Evolve-Filter-Relax (EFR) ROMs [18, 52, 51], Leray-ROMs, or more in general ROMs using filtering approaches inspired by Large Eddy Simulation (LES) [56, 31, 15].

Moreover, recently several researchers in the ROM community are putting their efforts into performing a system *closure*, by adding to the system data-driven terms aimed to close the gap between the system solution and a reference optimal solution [57, 3, 5].

The work presented in this manuscript has the goal of improving the performance of the standard POD-Galerkin ROMs, briefly recalled in 2.2, by the addition of some extra-terms into the reduced system.

The data-driven terms are of two fundamental types:

- (i) *physics-based* data-driven terms, that re-introduce the turbulence modeling inside the ROM, inspired on [19], presented in 2.3.1;
- (ii) *purely* data-driven terms, reintegrating the contributions of the neglected modes into the system, as done in [56, 31, 32], presented in 2.3.2.

The combination of the two strategies was already successfully applied to the test case of the periodic flow past a cylinder in [21].

The novelty of the present contribution consists of a machine-learning-based extension of the previous work to a parametrized setting, and on more challenging test cases. In particular, we show the numerical results for the periodic turbulent flow past a circular cylinder in Subsection 3.1, and for the unsteady channel-driven cavity flow in Subsection 3.2. In both test cases, different neural networks have been investigated to find the extra-terms (i) and (ii).

Finally, the discussion section 3.3 and the conclusive part 4 summarize the key results obtained in the contribution.

2. NUMERICAL METHODS

This Section is dedicated to the presentation of the numerical methods used in this project. In particular, it is divided in the following parts:

- the presentation of the Full Order Model (FOM) in Section 2.1, which is used to compute the *offline* solutions, named *snapshots*;
- a brief overview of the POD-Galerkin ROM approach in Section 2.2, which is the starting model of our analysis, and the Pressure Poisson Equation (PPE) stabilization technique;
- the machine learning techniques used to enhance the standard POD-Galerkin approach, in Section 2.3. We will briefly describe the *physics-based data-driven* approach in Section 2.3.1 and the *purely data-driven* approach in Section 2.3.2.

2.1. Full Order Model (FOM)

We call the fluid domain $\Omega \in \mathbb{R}^d$ with $d = 2$ (since we are considering only 2-dimensional domains), Γ its boundary. We indicate by $\boldsymbol{\mu}$ the flow parameters. In our specific test cases, $\boldsymbol{\mu} \in \mathbb{R}^2$, and it includes time $t \in [0, T]$ and the kinematic viscosity ν . $\mathbf{u} = \mathbf{u}(\mathbf{x}, \boldsymbol{\mu})$ is the flow velocity vector field, $p = p(\mathbf{x}, \boldsymbol{\mu})$ is the pressure scalar field normalized by the fluid density. In both the test cases we consider in the numerical results, the FOM is based on the Unsteady Reynolds–Averaged Navier–Stokes (URANS) formulation for incompressible flows, which consists of a time-averaged version of the Navier–Stokes equations.

The main hypothesis that characterizes the RANS approach is the *Reynolds decomposition* [40]. This theory is based on the assumption that each flow field \mathbf{s} can be expressed as the sum of its time averaged value, indicated as $\bar{\mathbf{s}}$, and fluctuating parts, indicated with \mathbf{s}' . Such mean has different definitions depending on the case of application. Classical choices are, for example, time averaging, averaging along homogeneous directions or ensemble averaging.

We briefly recall here the standard URANS formulation for the incompressible Navier-Stokes equations:

$$\begin{cases} \frac{\partial \bar{u}_i}{\partial x_i} = 0, \\ \bar{u}_j \frac{\partial \bar{u}_i}{\partial x_j} = -\frac{\partial \bar{p}}{\partial x_i} + \frac{\partial (2\nu \bar{\mathbf{E}}_{ij} - \mathcal{R}_{ij})}{\partial x_j}, \end{cases} \quad (1)$$

where the Einstein notation has been adopted, $\mathcal{R}_{ij} = \overline{u'_i u'_j}$ is the Reynolds stress tensor, and $\bar{\mathbf{E}}_{ij} = \frac{1}{2} \left(\frac{\partial \bar{u}_i}{\partial x_j} + \frac{\partial \bar{u}_j}{\partial x_i} \right)$ is the averaged strain rate tensor.

The URANS formulation in (1) needs to be coupled with a turbulence model to close system (1). In particular, we adopt the $\kappa - \omega$ *Shear Stress Transport* (SST) model [29].

This model belongs to the class of *eddy viscosity models*, which are based on the Boussinesq hypothesis, i.e. the turbulent stresses are related to the mean velocity gradients as follows:

$$-\mathcal{R}_{ij} = 2\nu_t \bar{\mathbf{E}}_{ij} - \frac{2}{3} \kappa \delta_{ij},$$

where $\kappa = \frac{1}{2}\overline{u'_i u'_i}$ is the turbulent kinetic energy and ν_t is the eddy viscosity. In general, in this case the URANS model is enriched with two additional transport equations, for κ and ω , respectively. For the complete model we refer the reader to the original paper [29], and the extended RANS model including the SST $\kappa - \omega$ equations can be found in [19].

The full order solutions of 1 are computed by means of the open-source software *OpenFOAM*, which employs a finite volume discretization of the URANS equations [34, 24].

Following the finite volume method, developed and implemented in [34, 24], the computational domain is discretized in polygonal control volumes and the partial differential equations 1 are integrated in each control volume and converted to algebraic equations. In particular, the volume integrals are converted into surface integrals by the divergence theorem, and discretized as sums of the fluxes at the boundary faces of the control volumes [34].

2.2. POD-Galerkin Reduced Order Models

In this section, we provide a brief overview of the standard POD-Galerkin ROM approach.

Once all the high-fidelity simulations are run, considering completed the offline stage, all the FOM snapshots, i.e., the FOM solutions for different parameter values $\{\boldsymbol{\mu}_j\}_{j=1}^{N_\mu}$, in our case for different time instances $\{t_i\}_{i=1}^{N_T}$ and for different viscosity values $\{\nu_k\}_{k=1}^{N_M}$, where $N_\mu = N_T \times N_M$. In particular, each parameter is $[t_i, \nu_k]$, $i = 1, \dots, N_T$, $k = 1, \dots, N_M$. The POD is then applied on the full order snapshots' matrices:

$$\mathcal{S}_u = \{\mathbf{u}(\mathbf{x}, \boldsymbol{\mu}_1), \dots, \mathbf{u}(\mathbf{x}, \boldsymbol{\mu}_{N_\mu})\} \in \mathbb{R}^{N_u^h \times N_\mu}, \quad \mathcal{S}_p = \{p(\mathbf{x}, \boldsymbol{\mu}_1), \dots, p(\mathbf{x}, \boldsymbol{\mu}_{N_\mu})\} \in \mathbb{R}^{N_p^h \times N_\mu}.$$

If we call N_c the number of cells of the mesh considered, $N_u^h = d N_c$ and $N_p^h = N_c$ are the numbers of spatial degrees of freedom for the velocity and pressure fields, respectively.

After the POD is applied to the snapshots' matrices, the following reduced POD spaces are found:

$$\mathbb{V}_{\text{POD}}^u = \text{span}\{[\phi_i]_{i=1}^{N_u}\}, \quad \mathbb{V}_{\text{POD}}^p = \text{span}\{[\chi_i]_{i=1}^{N_p}\}, \quad (2)$$

where $N_u \ll N_u^h$ and $N_p \ll N_p^h$, and $[\phi_i]_{i=1}^{N_u}$ and $[\chi_i]_{i=1}^{N_p}$ indicate the velocity and pressure POD modes, respectively.

The main hypothesis of the POD is that each field can be then approximated as a convex combination of its modes, namely:

$$\mathbf{u}(\mathbf{x}, \boldsymbol{\mu}) \approx \mathbf{u}_r(\mathbf{x}, \boldsymbol{\mu}) = \sum_{i=1}^{N_u} a_i(\boldsymbol{\mu}) \phi_i(\mathbf{x}), \quad p(\mathbf{x}, t) \approx p_r(\mathbf{x}, \boldsymbol{\mu}) = \sum_{i=1}^{N_p} b_i(\boldsymbol{\mu}) \chi_i(\mathbf{x}). \quad (3)$$

Supposing that the reduced fields provide an accurate approximation of the original snapshots, the reduced order system can be written in a compact form as:

$$\begin{cases} \mathbf{f}(\mathbf{a}, \mathbf{b}; \boldsymbol{\mu}) = \mathbf{0}, \\ \mathbf{c}(\mathbf{a}; \boldsymbol{\mu}) = \mathbf{0}. \end{cases} \quad (4)$$

In (4) and in the following parts of the manuscript we will omit the dependencies $\mathbf{a}(\boldsymbol{\mu})$ and $\mathbf{b}(\boldsymbol{\mu})$ for the sake of brevity.

The above-mentioned model represents a system of DAEs whose unknowns are the vectors of coefficients $\mathbf{a} = (\mathbf{a})_{i=1}^{N_u}$ (for the velocity), and $\mathbf{b} = (\mathbf{b})_{i=1}^{N_p}$ (for the pressure).

However, it may happen that the model (4) is not stable in terms of velocity-pressure coupling and this may lead to spurious oscillations, causing the residuals to increase as time evolves. For this reason, there exist in literature different stabilization approaches for the velocity-pressure coupling. Two of those approaches are the supremizer method (SUP-ROM) and the Pressure Poisson Equation approach (PPE-ROM). The first approach consists in enriching the velocity reduced space with additional modes named *supremizer modes*, which are directly computed either from the pressure modes (*exact* supremizer approach) or from the pressure snapshots (*approximated* supremizer approach) [45, 8, 49, 6]. The second method simply replaces the reduced continuity equation with a reduced version of the Pressure Poisson Equation, which is computed by taking the divergence of the conservation of the momentum equation [4, 48, 49, 36].

In this project, we choose to adopt the PPE-ROM stabilization for two specific reasons:

- (i) it relies on a dedicated pressure equation and it allows for the introduction of specific *pressure correction* terms only acting on the pressure accuracy, as will be specified in Section 2.3;
- (ii) it is consistent with velocity-pressure coupling at the FOM level.

In the case of PPE-ROMs we report here the standard POD-Galerkin ROM formulations, which we will refer to as *standard ROM*.

$$\begin{cases} \mathbf{M}\dot{\mathbf{a}} = \nu(\mathbf{B} + \mathbf{B}_T)\mathbf{a} - \mathbf{a}^T \mathbf{C} \mathbf{a} - \mathbf{H}\mathbf{b} + \tau \left(\sum_{k=1}^{N_{BC}} (U_{BC,k} \mathbf{D}^k - \mathbf{E}^k \mathbf{a}) \right), \\ \mathbf{D}\mathbf{b} + \mathbf{a}^T \mathbf{G} \mathbf{a} - \nu \mathbf{N} \mathbf{a} - \mathbf{L} = \mathbf{0}. \end{cases} \quad (5)$$

In the above formulation, the POD operators read as follows:

$$\begin{aligned} (\mathbf{M})_{ij} &= (\phi_i, \phi_j)_{L^2(\Omega)}, & (\mathbf{P})_{ij} &= (\chi_i, \nabla \cdot \phi_j)_{L^2(\Omega)}, & (\mathbf{B})_{ij} &= (\phi_i, \nabla \cdot \nabla \phi_j)_{L^2(\Omega)}, \\ (\mathbf{B}_T)_{ij} &= (\phi_i, \nabla \cdot (\nabla \phi_j)^T)_{L^2(\Omega)}, & (\mathbf{C})_{ijk} &= (\phi_i, \nabla \cdot (\phi_j \otimes \phi_k))_{L^2(\Omega)}, & (\mathbf{H})_{ij} &= (\phi_i, \nabla \chi_j)_{L^2(\Omega)}, \\ (\mathbf{D})_{ij} &= (\nabla \chi_i, \nabla \chi_j)_{L^2(\Omega)}, & (\mathbf{G})_{ijk} &= (\nabla \chi_i, \nabla \cdot (\phi_j \otimes \phi_k))_{L^2(\Omega)}, \\ (\mathbf{N})_{ij} &= (\mathbf{n} \times \nabla \chi_i, \nabla \phi_j)_{L^2(\Gamma)}, & (\mathbf{L})_{ij} &= (\chi_i, \mathbf{n} \cdot \mathbf{R}_t)_{L^2(\Gamma)}, \end{aligned} \quad (6)$$

vector \mathbf{n} is the normal unitary vector to the domain boundary.

Moreover, the additional term in the momentum equation is a *weak* enforcement of the non-homogeneous Dirichlet boundary conditions, according to the *penalty method*. The penalization factor, namely τ tuned through a sensitivity analysis on the specific problem considered [19, 50]. In general, bigger values of the penalization factor lead to a stronger enforcement of the boundary conditions. At the same time, large values of τ also lead to larger condition number for system (5) and, hence, to less stability.

The matrices \mathbf{E}^k and vectors \mathbf{D}^k are defined as follows:

$$(\mathbf{E}^k)_{ij} = (\phi_i, \phi_j)_{L^2(\Gamma_{D_k})}, \quad (\mathbf{D}^k)_i = (\phi_i)_{L^2(\Gamma_{D_k})}, \quad \text{for all } k = 1, \dots, N_{BC},$$

where Γ_{D_i} is the i -th boundary with non-homogeneous Dirichlet conditions, N_{BC} is the total number of boundaries where non-homogeneous Dirichlet boundary conditions are imposed.

We can finally rewrite the formulation in System (5) in the following compact form, which is inherited from the form in (4):

$$\begin{cases} \mathbf{f}(\mathbf{a}, \mathbf{b}; \boldsymbol{\mu}) = \mathbf{0}, \\ \mathbf{h}(\mathbf{a}, \mathbf{b}; \boldsymbol{\mu}) = \mathbf{0}, \end{cases} \quad (7)$$

where the expression $\mathbf{h}(\mathbf{a}, \mathbf{b}; \boldsymbol{\mu})$ includes all the already mentioned contributions of the PPE and replaces the continuity equation $\mathbf{c}(\mathbf{a}) = \mathbf{0}$ in (4).

Although the PPE-ROM approach is well-known in the POD-Galerkin framework to provide an efficient stabilization, it may fail in capturing the flow dynamics especially in unsteady and turbulent test cases, like the cases we will consider in Section 3. This motivates the following Section, describing the data-driven techniques used to improve the accuracy.

2.3. Machine-learning-enhanced Reduced Order Models

This part of the manuscript is dedicated to the description of the machine learning techniques adopted to enhance the ROM results. In particular, this Section is divided into two parts:

- the description of the models used to model the reduced approximation of the *eddy viscosity* field, which is here introduced to take into account the turbulent behaviour of the flow (section 2.3.1);
- the description of the models used to approximate the *correction/closure* terms added into the System (5) (section 2.3.2).

2.3.1 Physics-based data-driven methods

The main goal of this Section is to add the turbulence modeling inside the reduced formulation, building the so-called *physics-based data-driven model*. As specified in Section 2.1, the URANS approach used to model the FOM usually includes turbulence by using an *eddy viscosity* model. For instance, in our case we considered the SST $\kappa - \omega$ model, which adds to the URANS equations the transport equations for κ and ω .

It is important to highlight that only the projections of the momentum and the PPE equations are considered at the reduced order level. Since the projections of the κ and ω transport equations are not taken into account, it is important to include the turbulent viscosity modeling in the momentum and PPE equations.

Indeed, an approximation version of the eddy viscosity field can be modeled and included in the reduced system (5), as done in [19], as follows:

where $\eta_i(\mathbf{x})$ is the i -th eddy viscosity mode evaluated through a POD procedure, just as done for the velocity and pressure fields, $g_i(\boldsymbol{\mu})$ is the corresponding coefficient, N_{ν_t} is the *a-priori* selected number of modes retained for the eddy-viscosity field.

When using a PPE approach, the URANS system (1) at the full order level can be written as follows:

$$\left\{ \begin{array}{l} \frac{\partial \bar{\mathbf{u}}}{\partial t} + \nabla \cdot (\bar{\mathbf{u}} \otimes \bar{\mathbf{u}}) = \nabla \cdot [-\bar{p} \mathbf{I} + (\nu + \nu_t) (\nabla \bar{\mathbf{u}} + (\nabla \bar{\mathbf{u}})^T)] \quad \text{in } \Omega \times [0, T], \\ \Delta \bar{p} = -\nabla \cdot (\nabla \cdot (\bar{\mathbf{u}} \otimes \bar{\mathbf{u}})) + \nabla \cdot [\nabla \cdot (\nu_t (\nabla \bar{\mathbf{u}} + (\nabla \bar{\mathbf{u}})^T))] \quad \text{in } \Omega, \\ + \text{Boundary Conditions} \quad \text{on } \Gamma \times [0, T], \\ + \text{Initial Conditions} \quad \text{in } (\Omega, 0). \end{array} \right. \quad (8)$$

Consequently, the dynamical system (5) takes the following form:

$$\left\{ \begin{array}{l} \mathbf{M} \dot{\mathbf{a}} = \nu (\mathbf{B} + \mathbf{B}_T) \mathbf{a} - \mathbf{a}^T \mathbf{C} \mathbf{a} + \mathbf{g}^T (\mathbf{C}_{T1} + \mathbf{C}_{T2}) \mathbf{a} - \mathbf{H} \mathbf{b} + \tau \left(\sum_{k=1}^{N_{BC}} (U_{BC,k} \mathbf{D}^k - \mathbf{E}^k \mathbf{a}) \right), \\ \mathbf{D} \mathbf{b} + \mathbf{a}^T \mathbf{G} \mathbf{a} - \mathbf{g}^T (\mathbf{C}_{T3} + \mathbf{C}_{T4}) \mathbf{a} - \nu \mathbf{N} \mathbf{a} - \mathbf{L} = \mathbf{0}, \end{array} \right. \quad (9)$$

where:

$$\begin{aligned} (\mathbf{C}_{T1})_{ijk} &= (\phi_i, \eta_j \nabla \cdot \nabla \phi_k)_{L^2(\Omega)}, & (\mathbf{C}_{T2})_{ijk} &= (\phi_i, \nabla \cdot \eta_j (\nabla \phi_k)^T)_{L^2(\Omega)}, \\ (\mathbf{C}_{T3})_{ijk} &= (\nabla \chi_i, \eta_j \nabla \cdot \nabla \phi_k)_{L^2(\Omega)}, & (\mathbf{C}_{T4})_{ijk} &= (\nabla \chi_i, \nabla \cdot \eta_j (\nabla \phi_k)^T)_{L^2(\Omega)}. \end{aligned}$$

In the dynamical system defined in (9) the number of unknowns is N_u for the velocity, N_p for the pressure, and N_{ν_t} for the eddy viscosity. However, the number of equations is $N_u + N_p$. Thus, there are more unknowns than equations and the system is not closed. In order to close the systems, the eddy viscosity coefficients $[g_i(\boldsymbol{\mu})]_{i=1}^{N_{\nu_t}}$ can be computed considering the mapping $\mathbf{g} = \mathcal{G}(\mathbf{a}, \boldsymbol{\mu})$ through either *interpolation* [28, 30] or *regression* techniques. An interpolation technique was exploited in [19], following the POD-I approach [54, 53, 46]. In this paper, the mapping is a feed-forward fully-connected neural network whose loss function is the mean squared error (MSE) between the output of the neural network $\mathcal{G}(\mathbf{a}, \boldsymbol{\mu})$ and the known eddy viscosity coefficients $\mathbf{g}^{proj}(\boldsymbol{\mu})$ found from the POD procedure. The compact form of system (9) is:

$$\left\{ \begin{array}{l} \mathbf{f}(\mathbf{a}, \mathbf{b}, \mathbf{g}; \boldsymbol{\mu}) = \mathbf{0}, \\ \mathbf{h}(\mathbf{a}, \mathbf{b}, \mathbf{g}; \boldsymbol{\mu}) = \mathbf{0}. \end{array} \right. \quad (10)$$

2.3.2 Purely data-driven methods

The main goal here is to identify a strategy to model the *correction/closure* terms already exploited in previous works like [32, 33, 47, 3, 22, 14, 21], but in a parametric setting.

The procedure used is as follows.

1. Select a reduced dimension for the velocity, $r \equiv N_u$, and for the pressure, $q \equiv N_p$. The sum $r + q$ is the dimension of the reduced system (5).
2. Select two bigger dimensions $d > r$ and $h > q$, for instance in literature we have $d = kr$, $h = kq$, with k an integer.
3. Select one or more operators, that we name \mathcal{C} . For instance, if we only consider the non-linear operators in System (5) we obtain:

$$\mathcal{C}(\mathbf{a}) = \begin{bmatrix} \mathbf{a}^T \mathbf{C} \mathbf{a} \\ \mathbf{a}^T \mathbf{G} \mathbf{a} \end{bmatrix}. \quad (11)$$

4. Compute the term $\mathcal{C}(\mathbf{a}_d^{proj}) \in \mathbb{R}^{d+h}$:

$$\mathcal{C}(\mathbf{a}_d^{proj}) = \begin{bmatrix} (\mathbf{a}_d^{proj})^T \mathbf{C}_d \mathbf{a}_d^{proj} \\ (\mathbf{a}_d^{proj})^T \mathbf{G}_h \mathbf{a}_d^{proj} \end{bmatrix}, \quad (12)$$

where \mathbf{a}_d^{proj} is the velocity coefficients' vector found by directly projecting the field on the POD subspace of dimension d . The operators \mathbf{C}_d and \mathbf{G}_h are expressed as:

$$\begin{aligned} (\mathbf{C}_d)_{ijk} &= (\phi_i, \nabla \cdot (\phi_j \otimes \phi_k))_{L^2(\Omega)}, \quad i, j, k = 1, \dots, d, \\ (\mathbf{G}_h)_{ijk} &= (\nabla \chi_i, \nabla \cdot (\phi_j \otimes \phi_k))_{L^2(\Omega)}, \quad i = 1, \dots, h; j, k = 1, \dots, d. \end{aligned}$$

5. Compute the term $\mathcal{C}(\mathbf{a}_r^{proj}) \in \mathbb{R}^{r+q}$:

$$\mathcal{C}(\mathbf{a}_r^{proj}) = \begin{bmatrix} (\mathbf{a}_r^{proj})^T \mathbf{C} \mathbf{a}_r^{proj} \\ (\mathbf{a}_r^{proj})^T \mathbf{G} \mathbf{a}_r^{proj} \end{bmatrix}, \quad (13)$$

where \mathbf{a}_r^{proj} is the velocity coefficients' vector found by directly projecting the field on the POD subspace of dimension r . The operators \mathbf{C} and \mathbf{G} are the reduced operators appearing in (5) and already defined in (6).

6. Compute the *exact* correction term as follows:

$$\boldsymbol{\tau}^{exact} = \overline{\mathcal{C}(\mathbf{a}_d^{proj})}^r - \mathcal{C}(\mathbf{a}_r^{proj}), \quad (14)$$

where $\overline{(\cdot)}^r$ acts like a filter and indicates that only the first r components should be retained. In our example, we will have $\boldsymbol{\tau}^{exact} \in \mathbb{R}^{r+q}$:

$$\boldsymbol{\tau}^{exact} = \begin{bmatrix} \overline{(\mathbf{a}_d^{proj})^T \mathbf{C}_d \mathbf{a}_d^{proj}}^r - (\mathbf{a}_r^{proj})^T \mathbf{C} \mathbf{a}_r^{proj} \\ \overline{(\mathbf{a}_d^{proj})^T \mathbf{G}_p \mathbf{a}_d^{proj}}^q - (\mathbf{a}_r^{proj})^T \mathbf{G} \mathbf{a}_r^{proj} \end{bmatrix}, \quad (15)$$

where we retain the first r and q components for the first and second term, respectively.

7. Finally, we have to choose a *model* \mathcal{M} able to approximate with good accuracy the exact correction term, also for unseen configurations, namely time and/or parameter extrapolation. In particular: $\boldsymbol{\tau}^{approx} = \boldsymbol{\tau}^{approx}(\mathbf{a}, \mathbf{b}, \boldsymbol{\mu}) = \mathcal{M}(\mathbf{a}, \mathbf{b}, \boldsymbol{\mu})$, where $\boldsymbol{\mu}$ includes the parameters of the test case taken into account. Some of the possible choices to model the mapping \mathcal{M} are the following.

- Choose an *ansatz*, for example a quadratic ansatz with respect to the coefficients' vectors:

$$\mathcal{M}(\mathbf{a}, \mathbf{b}) = \tilde{\mathbf{A}} \begin{bmatrix} \mathbf{a} \\ \mathbf{b} \end{bmatrix} + [\mathbf{a}^T \quad \mathbf{b}^T] \tilde{\mathbf{B}} \begin{bmatrix} \mathbf{a} \\ \mathbf{b} \end{bmatrix}. \quad (16)$$

where the matrix $\tilde{\mathbf{A}} \in \mathbb{R}^{(r+q) \times (r+q)}$ and the operator $\tilde{\mathbf{B}} \in \mathbb{R}^{(r+q) \times (r+q) \times (r+q)}$. This approach is easily addressed in time-dependent problems by solving a minimization problem:

$$\tilde{\mathbf{A}}, \tilde{\mathbf{B}} = \arg \min_{\mathbf{A}, \mathbf{B}} \left(\sum_{j=1}^M \left\| \mathbf{A} \begin{bmatrix} (\mathbf{a}_r^{proj}(t_j))^T \\ (\mathbf{b}_q^{proj}(t_j))^T \end{bmatrix} + [\mathbf{a}_r^{proj}(t_j) \quad \mathbf{b}_q^{proj}(t_j)] \mathbf{B} \begin{bmatrix} \mathbf{a}_r^{proj}(t_j) \\ \mathbf{b}_q^{proj}(t_j) \end{bmatrix} - \boldsymbol{\tau}^{exact}(t_j) \right\|^2 \right). \quad (17)$$

In previous works, like [33, 32, 21, 22], the minimization problem (17) is typically rewritten as a least squares problem. However, this can be done if time is the only parameter of the problem. Indeed, matrices $\tilde{\mathbf{A}}$ and $\tilde{\mathbf{B}}$ does not depend on time. Parametric test cases require more advanced mappings depending also on the remaining parameter(s).

- Train a *neural network* (NN), which takes as input the coefficients and the parameters of the problem $(\mathbf{a}, \mathbf{b}, \boldsymbol{\mu})$ and gives as output the approximated correction coefficients $\boldsymbol{\tau}^{approx}$. In this case, the mapping \mathcal{M} can be modeled considering different architectures, like a feed-forward fully-connected NN or a recurrent neural network, for instance a Long-Short Term Memory (LSTM). Moreover, also other *ad-hoc* architectures can be created to model the initial mapping, depending on the test case we are considering, as we will see in the results' section 3. The comparisons among the results obtained with the different neural networks are reported in the numerical results' Section 3, while the details on the architectures are reported in the supplementary parts A.1 and A.2, for test case \mathbf{a} and \mathbf{b} , respectively. This second approach is suitable for test case that are only time-dependent, but also for problems depending on more parameters, whose dependency is easily addressed by adding the parameters as input to the neural network.

When we employ a reduced eddy-viscosity model, as in (10), the operator \mathcal{C} can also include the turbulence contributions, namely terms $\mathbf{g}^T(\mathbf{C}_{T1} + \mathbf{C}_{T2})\mathbf{a}$ and $\mathbf{g}^T(\mathbf{C}_{T3} + \mathbf{C}_{T4})\mathbf{a}$.

Moreover, as in the previous works [22, 21], we identify the first r elements of the correction term $\boldsymbol{\tau} = \mathcal{M}(\mathbf{a}, \mathbf{b}, \boldsymbol{\mu})$ as the *velocity* correction, whereas the last q components are identifies as *pressure* correction. Hence, the $\boldsymbol{\tau}$ vector can be decomposed as $(\boldsymbol{\tau}_u, \boldsymbol{\tau}_p)$, where $\boldsymbol{\tau}_u \in \mathbb{R}^r$ and $\boldsymbol{\tau}_p \in \mathbb{R}^q$.

We are finally able to write the so-called *hybrid data-driven ROM*, which combines the physics-based and the purely data-driven based approaches. Its final compact formulation reads as follows:

$$\begin{cases} \mathbf{f}(\mathbf{a}, \mathbf{b}, \mathbf{g}; \boldsymbol{\mu}) + \boldsymbol{\tau}_u(\mathbf{a}, \mathbf{b}, \boldsymbol{\mu}) = \mathbf{0}, \\ \mathbf{h}(\mathbf{a}, \mathbf{b}, \mathbf{g}; \boldsymbol{\mu}) + \boldsymbol{\tau}_p(\mathbf{a}, \mathbf{b}, \boldsymbol{\mu}) = \mathbf{0}. \end{cases} \quad (18)$$

In particular, when we consider a *purely data-driven* approach, the exact correction $\boldsymbol{\tau}^{exact}$ considered in Step 6. is computed considered all the operators in the reduced system (5). When considering a *hybrid data-driven* approach, we include in the exact correction also the contribution depending on the reduced eddy viscosity \mathbf{g} .

It is important to remark that in this case the reduced eddy viscosity is not an input to the mapping \mathcal{M} but it is only embedded in the exact correction.

3. NUMERICAL RESULTS

In this paper, we test all the numerical methods presented in 2 on two different test cases:

- (a) the periodic flow past a circular cylinder;
- (b) the channel-driven cavity flow.

In both test cases, we consider as parameters both time and the viscosity value, i.e. the Reynolds number. In particular, we consider three different sets of snapshots for training and testing the reduced order models, that are represented in Figure 2 and specified in Table 1, for both the test cases. In particular, we use the following notation:

- T_{offline} and $\mathcal{N}_{\text{train}}$: the time window and set of viscosities, respectively, used to collect the snapshots for the parametric POD. In the test cases we consider, the collected data are also used to train the neural networks exploited to compute the data-driven terms;
- T_{online} and $\mathcal{N}_{\text{test}}$: the time window and set of viscosities, respectively, used to run the online simulations. These sets are used to test the parametric data-driven approaches in different extrapolation settings for both parameters.

Test case (a)	$T_{\text{offline}}[\text{s}]$	[20, 22]
	$T_{\text{online}}[\text{s}]$	[20, 28]
	$\mathcal{N}_{\text{train}}[\text{m}^2/\text{s}]$	$\{8,33 \times 10^{-5}; 1 \times 10^{-4}; 1,25 \times 10^{-4}; 1,67 \times 10^{-4}; 2,5 \times 10^{-4}\}$
	$\mathcal{N}_{\text{test}}[\text{m}^2/\text{s}]$	$\{7,69 \times 10^{-5}; 1,15 \times 10^{-4}; 3,33 \times 10^{-4}\}$
Test case (b)	$T_{\text{offline}}[\text{s}]$	[5, 15]
	$T_{\text{online}}[\text{s}]$	[5, 20]
	$\mathcal{N}_{\text{train}}[\text{m}^2/\text{s}]$	$\{5 \times 10^{-6}; 1 \times 10^{-5}; 2 \times 10^{-5}; 4 \times 10^{-5}; 1 \times 10^{-4}\}$
	$\mathcal{N}_{\text{test}}[\text{m}^2/\text{s}]$	$\{4 \times 10^{-6}; 7 \times 10^{-6}; 1,25 \times 10^{-4}\}$

Table 1: Different sets used to train and test the data-driven ROMs for both test cases.

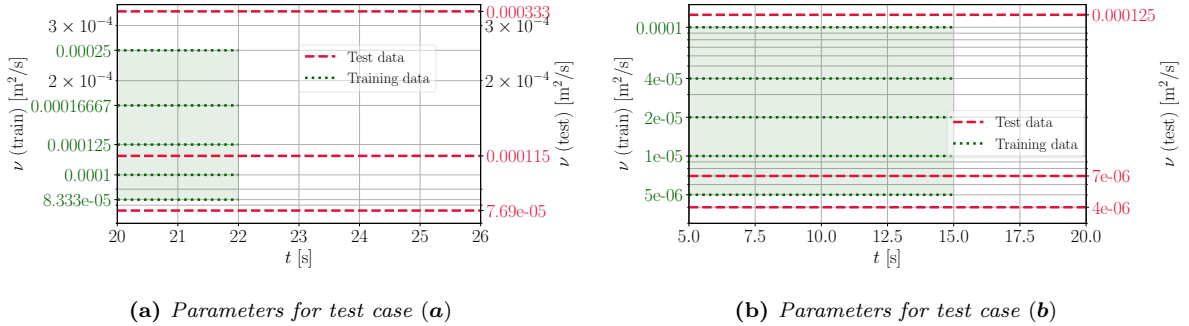


Figure 2: Graphical representations of the sets of parameters used in the offline stage (T_{offline} and $\mathcal{N}_{\text{train}}$), in green, and in the online stage (T_{online} and $\mathcal{N}_{\text{test}}$), in red. The green shadow describes the accessible offline/training area. The parameters are also specified in Table 1.

Moreover, we specify that we collect the snapshots every $\Delta t_{\text{offline}} = \Delta t_{\text{online}} = 4 \times 10^{-3}$ s for test case (a), and every $\Delta t_{\text{offline}} = \Delta t_{\text{online}} = 0,05$ s for test case (b).

The present Section is divided into two parts, one for each test case, and in both Subsections we focus on the following aspects:

- (i) Description of the FOM, POD eigenvalues decay, and selection of a reduced number of modes for the online stage;
- (ii) Neural networks' predictions of the data-driven correction terms;

(iii) Comparison among standard ROM and DD-ROMs in terms of relative L^2 errors of the velocity and pressure fields with respect to the high-fidelity solutions;

(iv) Graphical representation of the results at the final online time instance.

In the analysis of step (ii), we consider multiple neural networks with the same architecture but trained with different (random) weights initialization. Hence, we will show the performance of the regression models by displaying the average prediction (on all the pre-trained networks), and the true coefficients, namely the coefficients obtained by projection. We will also include the confidence interval of our model. We introduce the following notation: $\mathbf{s}^{\nu^*}(t) = \mathbf{s}(t; \nu^*)$ represents the full-order field of interest at the viscosity value ν^* and evolving in time, $\tilde{\mathbf{s}}$ indicates the ROM approximation of the field. In particular, in our case the fields are velocity or pressure: $\mathbf{s} = \mathbf{u}$ or $\mathbf{s} = p$. Following this notation, the 99.7% confidence interval $\mathcal{I}_{99.7\%}$ is computed as:

$$\mathcal{I}_{99.7\%}(t) = [i_-(t), i_+(t)], \text{ where } i_{\pm}(t) = \frac{\mu(\tilde{\mathbf{s}}^{\nu^*}(t)) \pm 3\sigma(\tilde{\mathbf{s}}^{\nu^*}(t))}{N_{\text{networks}}}, \quad (19)$$

where N_{networks} is the number of networks considered for the statistics in our case 10. The confidence interval reported in (19) is well-defined under the assumption of a Gaussian distribution. In particular, the difference among the N_{networks} models considered is the (random) initialization of the weights.

For what concerns step (iii), the expression of the time-dependent relative errors used to compare the ROMs performances is computed as follows.

$$\mathcal{E}_s^{\nu^*}(t) = \frac{\|\tilde{\mathbf{s}}^{\nu^*}(t) - \mathbf{s}^{\nu^*}(t)\|_{L^2(\Omega)}}{\|\mathbf{s}^{\nu^*}(t)\|_{L^2(\Omega)}}. \quad (20)$$

Also in this case, when dealing with DD-ROMs we will represent the statistics, namely the accuracy obtained considering in System (18) the averaged prediction of the neural networks, and the corresponding confidence interval.

3.1. Test case **a**: periodic flow past a cylinder

The periodic flow past a circular cylinder is a wide-known benchmark in fluid dynamics and in the field of reduced order modeling. In this Section we will focus on a parametric version of this test case, where the parameter considered is the viscosity that indirectly parametrizes the Reynolds number.

3.1.1 Offline stage

The domain and mesh for this test case are represented in Figure 3. Following the notation in the above-mentioned Figure, the boundary conditions read as follows.

$$\text{On } \partial\Omega_{in} : \begin{cases} \mathbf{u} = (U_{in}, 0), \\ \nabla p \cdot \mathbf{n} = 0; \end{cases} \quad \text{On } \partial\Omega_T \cup \partial\Omega_B : \begin{cases} \mathbf{u} \cdot \mathbf{n} = 0, \\ \nabla p \cdot \mathbf{n} = 0; \end{cases}$$

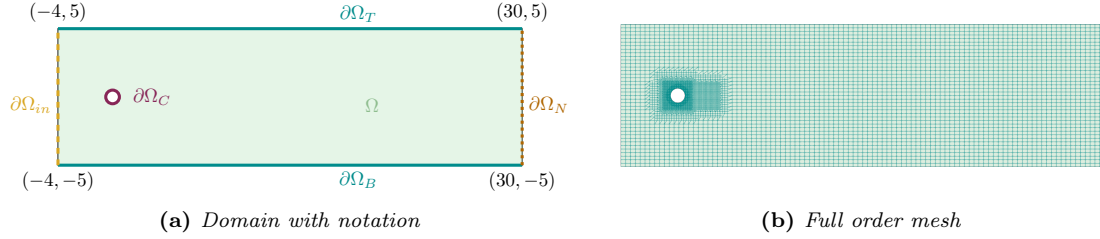


Figure 3: The domain and full order mesh considered for the periodic flow around a circular cylinder.

$$\text{On } \partial\Omega_N : \begin{cases} \nabla \mathbf{u} \cdot \mathbf{n} = 0, \\ p = 0; \end{cases} \quad \text{On } \partial\Omega_C : \begin{cases} \mathbf{u} = \mathbf{0}, \\ \nabla p \cdot \mathbf{n} = 0. \end{cases}$$

The time and parameter ranges considered to run the FOM and collect the POD snapshots have been introduced in Figure 2. Moreover, we collect a total amount of 500 snapshots for each viscosity value, for a total of 2500 snapshots. The snapshots are taken every 0,004s, the POD cumulative eigenvalues and the corresponding decay are represented in Figure 4. We can see a fast decay, especially for the velocity field. However, as we will see in the following part, the standard POD-Galerkin approach is characterized by lack of accuracy in the *marginally-resolved* regime, even if the number of modes considered is enough to capture the dynamics of the problem.

We decide to focus our analysis on a number of modes $N_u = N_{v_t} = r = 3$ and $N_p = q = 3$, namely in the *marginally-resolved* regime.

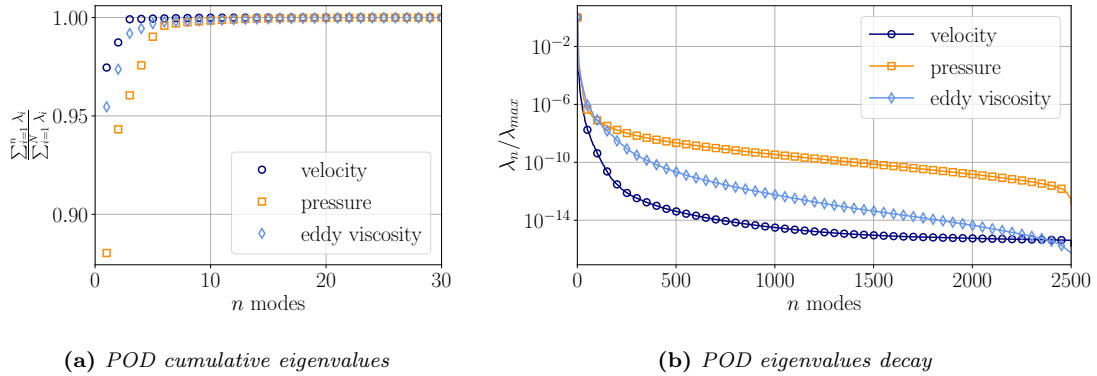


Figure 4: Cumulative eigenvalues and eigenvalues decay for the test case **a**.

3.1.2 Neural networks' performance

We focus here on the analysis of the accuracy of the neural networks used to compute both the *eddy viscosity* and the *correction* coefficients.

For what concerns the eddy viscosity coefficients, we consider as mapping $\mathcal{G}(\mathbf{a}, \nu, t)$ a multi-layer perceptron neural network, whose hyper-parameters' details can be found in the supplementary results in Section A.1.

Figure 5 shows the averaged prediction of the neural networks considered for the \mathcal{G} mapping, the corresponding confidence interval, and the exact coefficients. The prediction is here computed for a viscosity value in the train set $\mathcal{N}_{\text{train}}$ and for the same time window considered offline for collecting the POD snapshots. We can notice that the neural network has a good performance, since the prediction is close to the truth and the confidence interval is small. In particular, the performance is better for the eddy viscosity coefficients g_1 and g_2 than for the first component g_0 . However, this would not affect the results in terms of accuracy, as we will show in the analysis in 3.1.3.

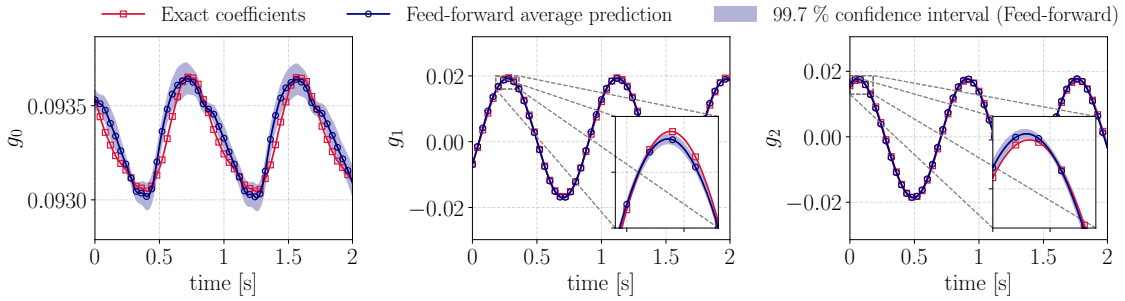


Figure 5: Eddy viscosity coefficients for $\nu = 8,33 \times 10^{-5} \text{ m s}^{-1}$ (in $\mathcal{N}_{\text{train}}$): neural networks predictions' average and corresponding confidence interval, and POD projected exact coefficients.

Figures 6 and 7 represent the performance of three different types of neural networks considered for the mapping \mathcal{M} , on two different training viscosities. In particular, we named the networks as:

- Feed-forward($\mathbf{a}, \mathbf{b}, \nu, t$), where ($\mathbf{a}, \mathbf{b}, \nu, t$) are the inputs, with a multi-layer perceptron standard architecture;
- LSTM($\mathbf{a}, \mathbf{b}, \nu$), where the time parameter is not considered since it is already embedded in the Long-Short Term Memory framework;
- SinNN(ν, t), which is an *ad-hoc* architecture, presented in the supplementary part, in Figure 22. It is inspired by the fact that the coefficients are in our case periodic, as can be seen from the eddy viscosity coefficients in Figure 5. Hence, the periodicity is integrated in the network by adding sinusoidal expressions in it.

The hyperparameters of the above-mentioned neural networks are reported in Section A.1.

From the comparison between Figures 6 and 7, it can be seen that the shape of the first coefficient of τ_u is more complex in 7. Therefore, also the prediction of the neural network is less accurate for this specific parameter. Moreover, the correction coefficients represented in these Figures also include the eddy viscosity contributions, but similar considerations can be withdrawn in the case not including the turbulent terms.

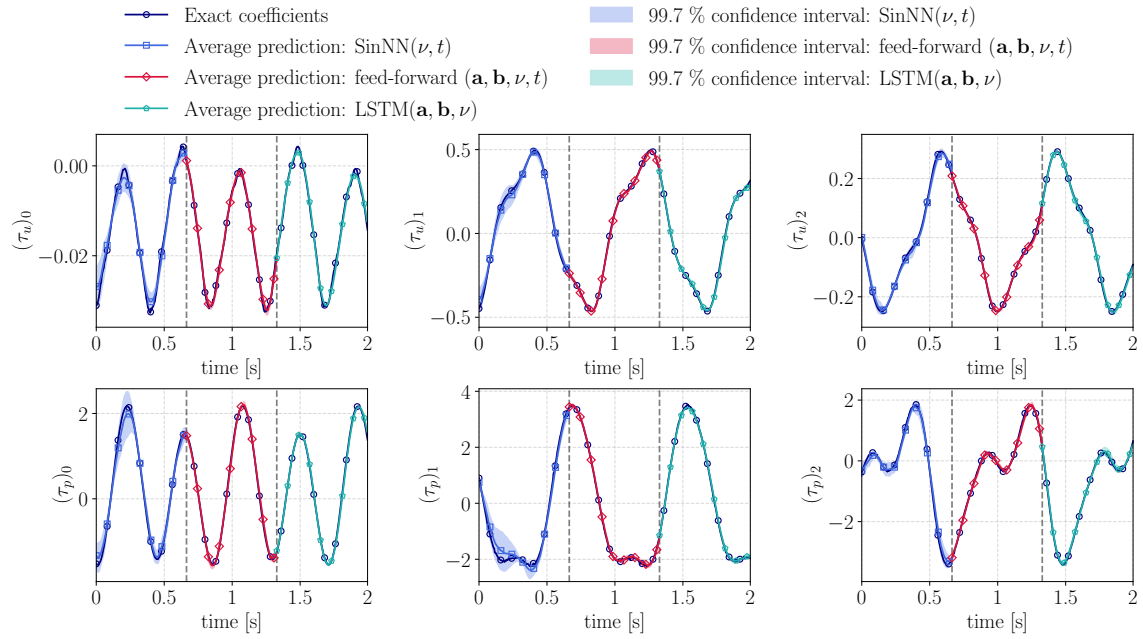


Figure 6: Correction terms' coefficients for $\nu = 8,33 \times 10^{-5} \text{ m s}^{-1}$ (in \mathcal{N}_{train}): neural networks predictions' average and corresponding confidence interval, and POD projected exact coefficients.

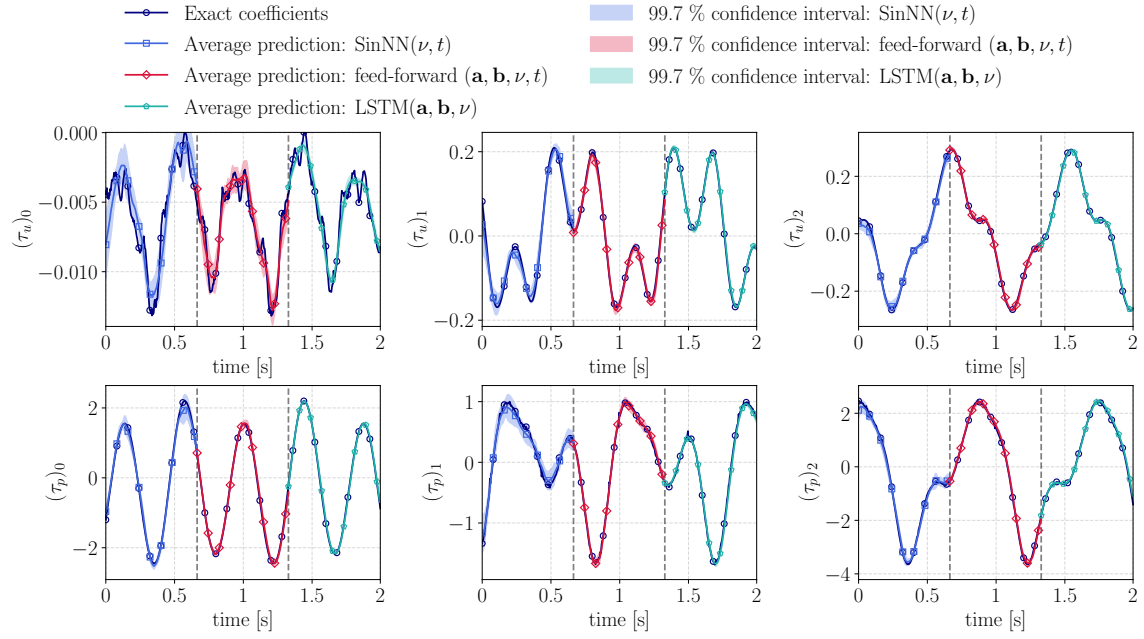


Figure 7: Correction terms' coefficients for $\nu = 1,25 \times 10^{-4} \text{ m s}^{-1}$ (in $\mathcal{N}_{\text{train}}$): neural networks predictions' average and corresponding confidence interval, and POD projected exact coefficients.

3.1.3 DD-ROMs performance

Figures 8 and 9 show the relative errors obtained with all the DD-ROMs here considered, making a comparison with the standard ROM and with the reconstruction error.

We report also the result of the DD-ROM obtained inserting in the reduced system (18) the *exact* correction term. From now on we will call this model the *exact purely DD-ROM* or *exact hybrid DD-ROM*, depending if the turbulence is included or not.

The viscosity parameter is a test parameter internal to the range considered for collecting the snapshots. Moreover, the online simulation is run until 6 seconds, namely in a time extrapolation regime, since the snapshots are collected in the window $[0, 2]$ s.

If we consider the purely DD-ROM (Figure 8), all the models slightly improve the results of the standard ROM. In particular, the LSTM outperforms both the exact purely DD-ROM and the standard ROM.

Indeed, the mapping \mathcal{M} is built such that its output is as close as possible to the exact correction, but the final DD-ROM accuracy may also be better than the exact model.

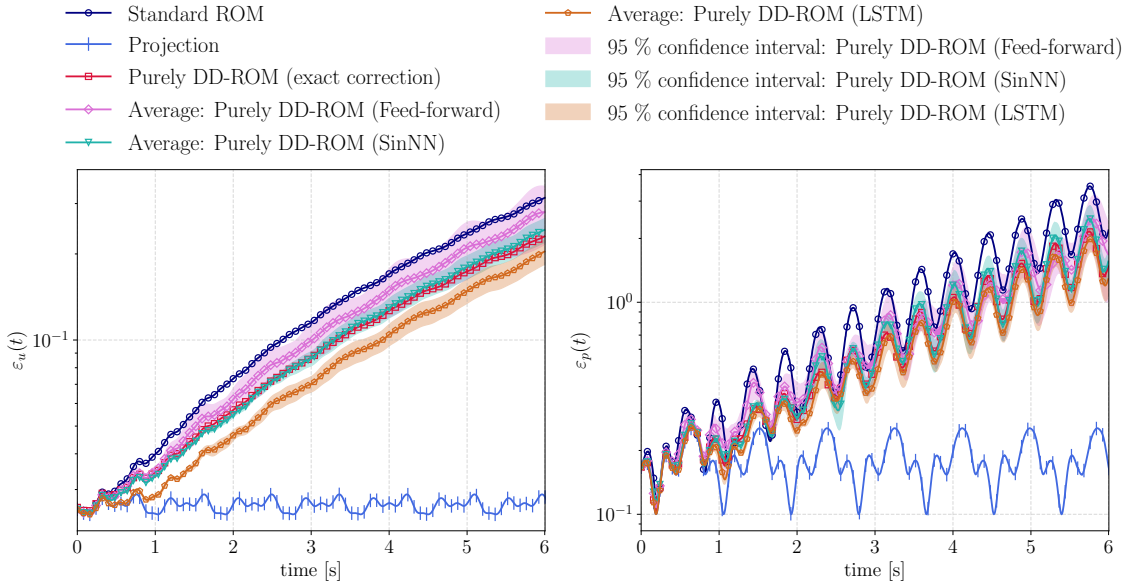


Figure 8: Relative errors for $\nu \in \mathcal{N}_{test}$ (inside the train dataset range) for the pressure and the velocity magnitude fields, for the purely DD-ROMs, standard POD-Galerkin ROMs. The reconstruction error is here also represented.

Figure 9 shows that the hybrid DD-ROM significantly improves the standard ROM results in an unseen setting for both time and viscosity. The LSTM is the best-performing machine learning algorithm for this test parameter. Indeed, the average prediction of the LSTM leads to an accuracy close to the reconstruction error and to the exact hybrid DD-ROM. Moreover, the model provides a more confident prediction than the others, since the confidence interval is smaller than the others. In addition, the SinNN has the worst performance among the machine learning model considered.

The reason for this fact may be that the SinNN does not take as inputs the velocity coefficients. Hence, it does not take into account the evolution of the dynamics leading to a worse performance in a test setting.

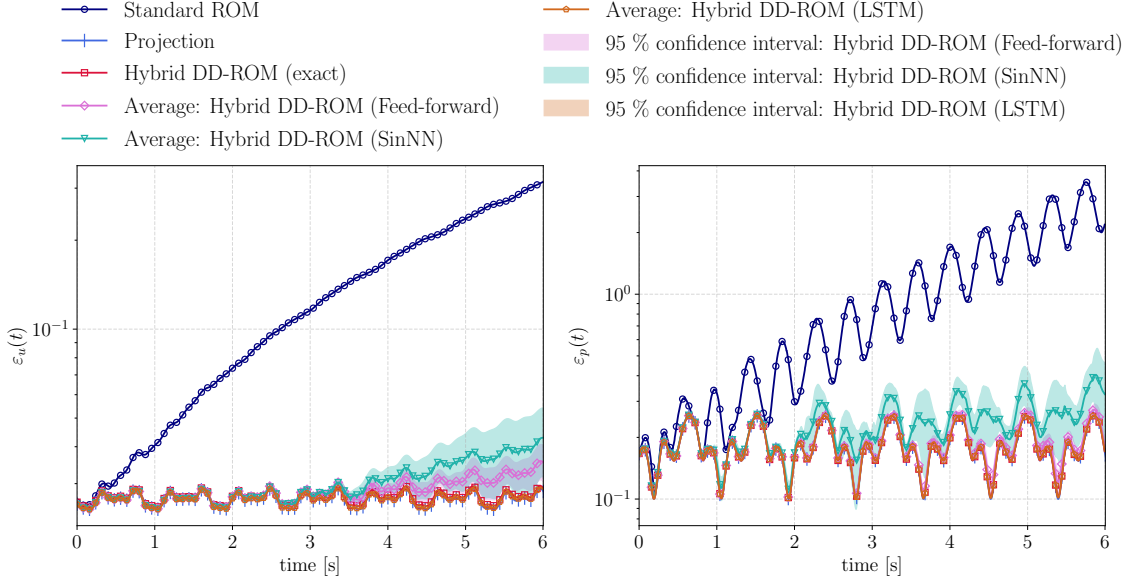


Figure 9: Relative errors for $\nu \in \mathcal{N}_{test}$, $\nu = 1,15 \times 10^{-4} \text{ m s}^{-1}$ for the pressure and the velocity magnitude fields, for the physics-based DD-ROMs, hybrid DD-ROMs, standard POD-Galerkin ROMs. The reconstruction error is here also represented.

For a global comparison of the different ROM methods, we refer to Figure 10, showing the integrals of the relative errors over the online time window [20, 26] s, for test viscosity values. The performance of all the methods is better for $\nu = 1,15 \times 10^{-4} \text{ m}^2/\text{s}$ since it is within the parameters' range considered for the POD. All the hybrid DD-ROM models outperform the standard approach, but the most accurate methods are the standard multi-layer perceptron and the LSTM, as previously pointed out.

3.1.4 Graphical results

Figures 11 and 12 show a graphical comparison of the velocity and pressure fields, respectively, at the final instance of the online simulation.

The POD-Galerkin ROM reconstruction leads to poor approximations in the region near the cylinder, for both the pressure and the velocity field. This may result in inaccurate predictions of the force fields, like the drag and the lift acting on the cylinder. On the other hand, as pointed out in Section 3.1.3, the hybrid models are significantly closer to the full-order solution. However, the SinNN is less accurate around the cylinder, as previously shown in the errors' plots.

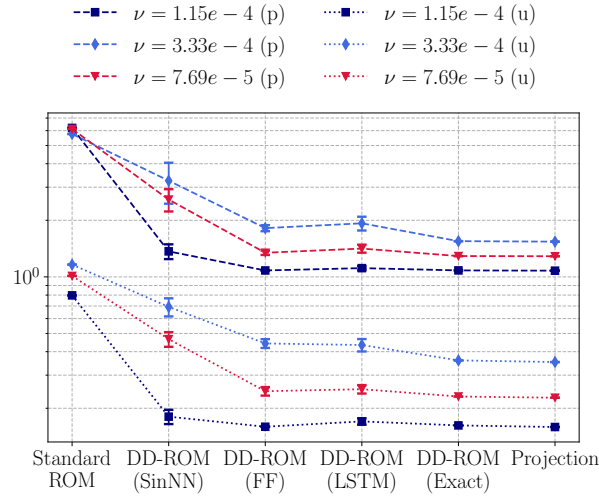


Figure 10: Integrals of relative errors over time for $\nu \in \mathcal{N}_{test}$ for the pressure and the velocity magnitude fields, in the standard ROM, hybrid DD-ROMs, and for the projection.

3.2. Test case **b**: flow in a channel-driven cavity

The unsteady case of the flow inside a cavity-shaped channel is characterized by a different behavior to the first test case described in 3.1. Also in this case, we consider a parametrized setup w.r.t. the Reynolds number.

3.2.1 Offline stage

In Figure 13 we represent the domain and the mesh considered in the FOM analysis.

Employing the notation in Figure 13, we consider the following boundary conditions:

$$\begin{aligned} \text{On } \partial\Omega_T : \begin{cases} \nabla \mathbf{u} \cdot \mathbf{n} = 0, \\ \nabla p \cdot \mathbf{n} = 0; \end{cases} & \quad \text{On } \partial\Omega_B : \begin{cases} \mathbf{u} = \mathbf{0}, \\ \nabla p \cdot \mathbf{n} = 0 \end{cases} \\ \text{On } \partial\Omega_{in} : \begin{cases} \mathbf{u} = (U_{in}^b, 0), \\ \nabla p \cdot \mathbf{n} = 0; \end{cases} & \quad \text{On } \partial\Omega_N : \begin{cases} \nabla \mathbf{u} \cdot \mathbf{n} = 0, \\ p = 0. \end{cases} \end{aligned}$$

For the POD we consider the viscosity range specified in Figure 2, with a corresponding Reynolds number in range $[1 \times 10^3, 2 \times 10^4]$. The time snapshots are retained every 0,05 seconds in the time interval of 10 seconds, for a total amount of snapshots of 1000, namely 200 for each FOM simulation.

Figure 14 shows the cumulative eigenvalues and the eigenvalues decay of the POD for all the fields considered. The Figure shows a slower decay than in the first test case (Figure 4). Indeed, this second test case is not periodic leading to a more challenging setting.

We decide to focus our analysis on a number of modes $N_u = N_{v_t} = r = 2$ and $N_p = q = 4$, namely in the *marginally-resolved* regime.

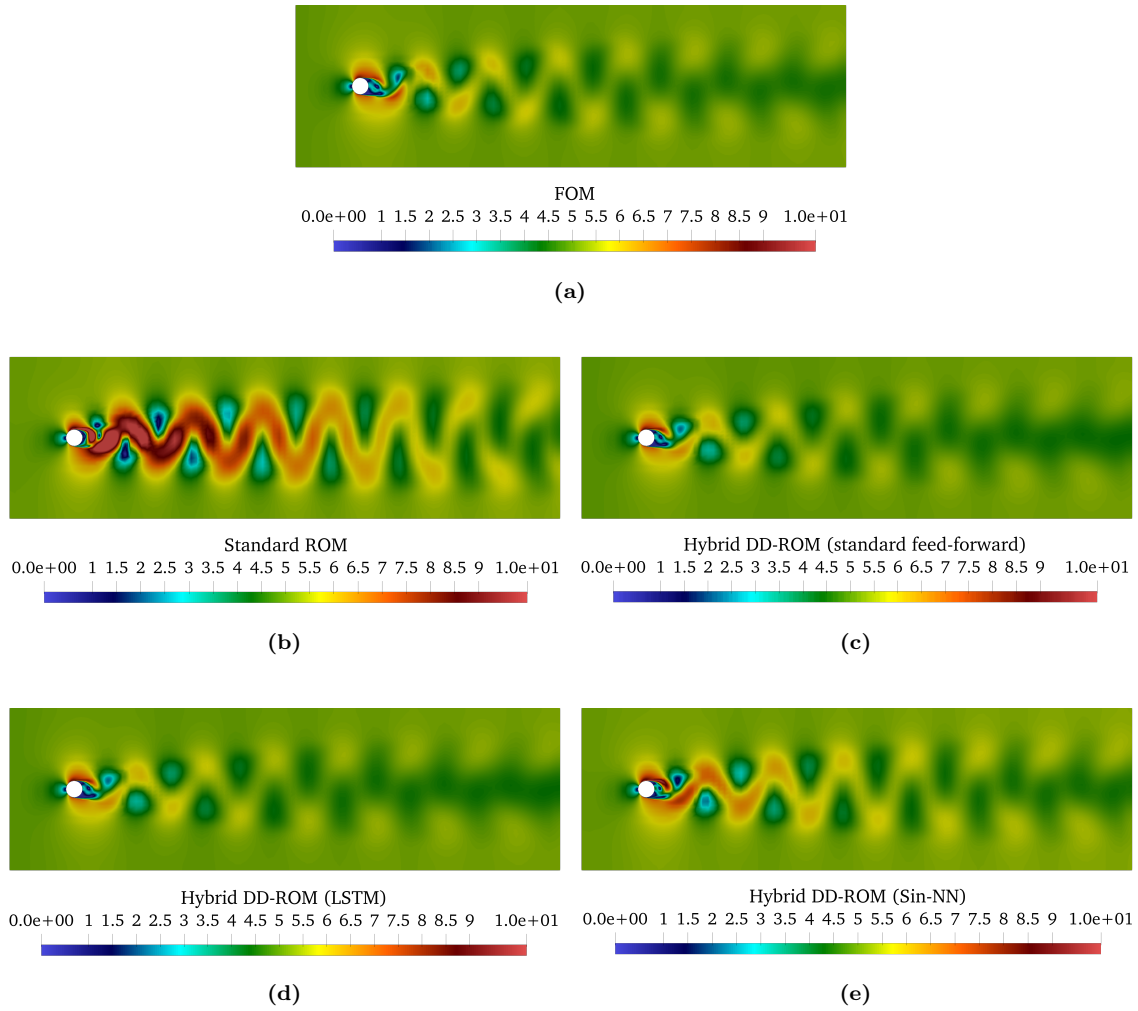


Figure 11: *Velocity magnitude fields at final instant of ROM.*

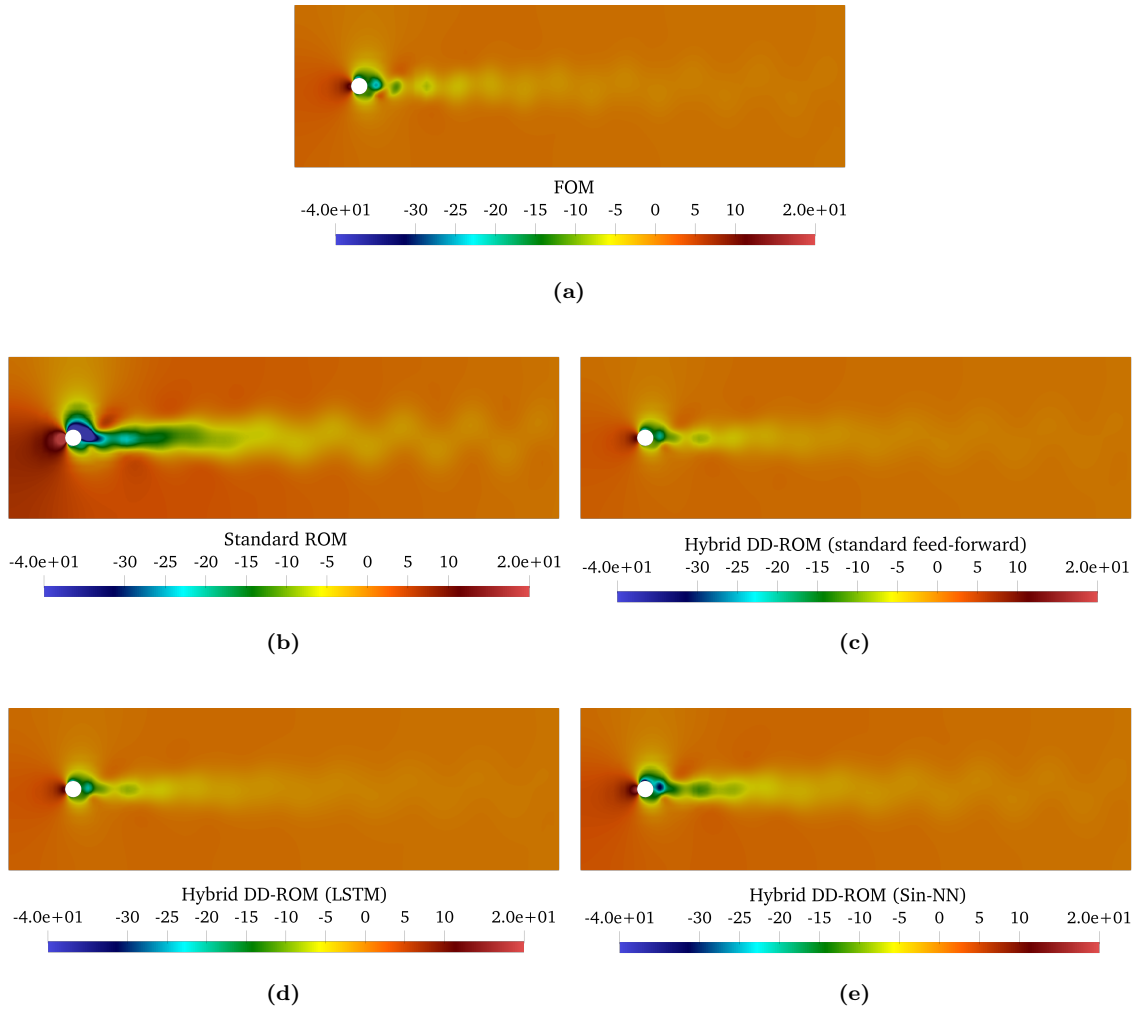


Figure 12: *Pressure fields at final instant of ROM.*

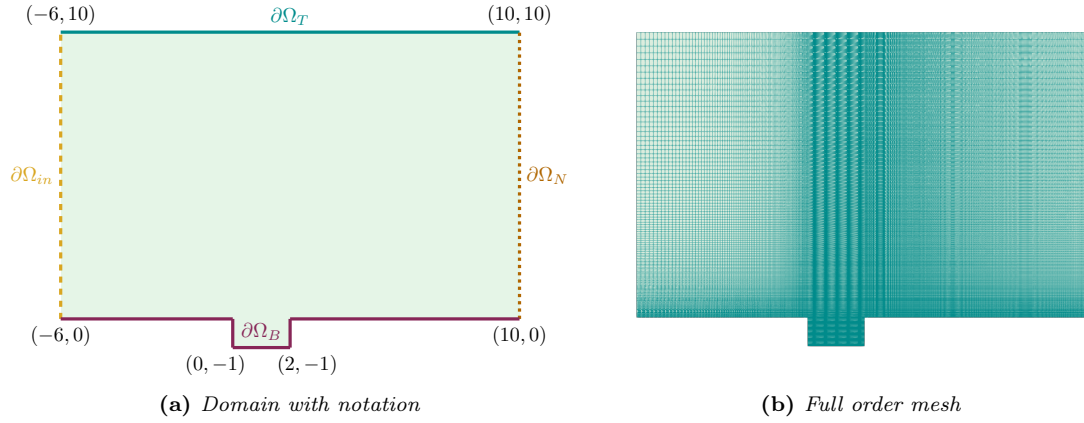


Figure 13: The domain and full order mesh considered for the channel-driven flow test case.

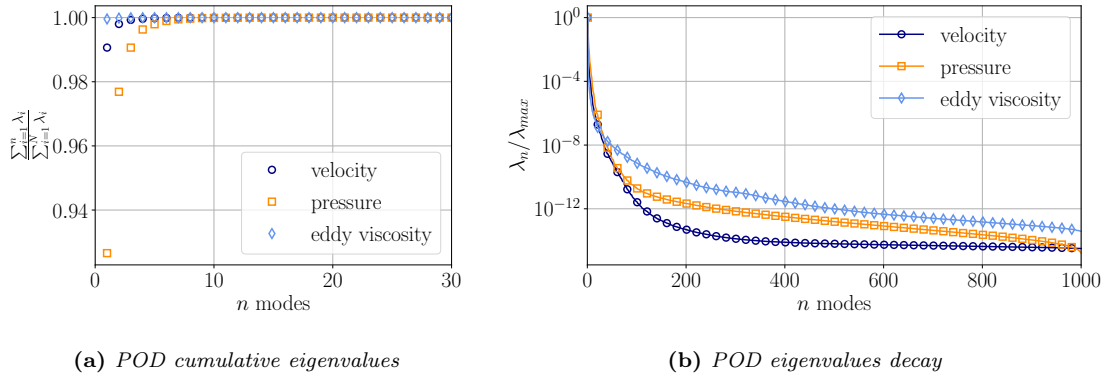


Figure 14: Cumulative eigenvalues and eigenvalues decay for test case **b**.

3.2.2 Neural networks' performance

As already done in Subsection 3.1.2, the goal of this part is to show the performance of the neural networks used to predict both the *eddy viscosity* coefficients and the *correction* coefficients.

In particular, the first mapping $\mathcal{G}(\mathbf{a}, \nu, t)$ is built, as in the first test case, with a multi-layer perceptron architecture. Figure 15 represents the performance of the machine learning model considered in a training setup. The resulting average prediction is accurate and the confidence interval is very small in both the coefficients g_0 and g_1 . Moreover, we notice that the trend of the coefficients is not periodic, but it is monotone, differently from test case **a**.

For what concerns the mapping \mathcal{M} we only take into account the pressure corrections τ_p , since the velocity approximation has not a relevant contribution in this case. For this reason, in the networks we will not take into account the velocity coefficients \mathbf{a} as input.

Figure 16 shows the performance of three different types of neural networks for mapping \mathcal{M} . In particular, we named the networks as:

- Feed-forward(\mathbf{b}, ν, t), where (\mathbf{b}, ν, t) are the inputs, with a multi-layer perceptron standard architecture;
- LSTM(\mathbf{b}, ν), where the time parameter is not considered since it is already embedded in the Long-Short Term Memory framework;
- Feed-forward(ν, t), where (ν, t) are the only inputs. We chose to test this model for the simple monotone trend in time of the coefficients.

The sequence length used for the LSTM, i.e. the entity of time memory, is 20 time steps, corresponding to 1 second of simulation.

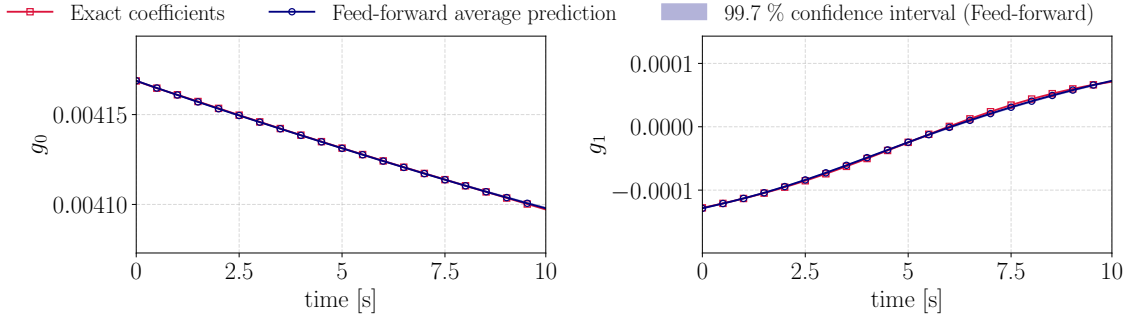


Figure 15: *Eddy viscosity coefficients for $\nu = 5 \times 10^{-6} \text{ m}^2/\text{s}$ (in \mathcal{N}_{train}): neural networks predictions' average and POD projected exact coefficients.*

3.2.3 DD-ROMs performance

We decide in this Section to focus only on the hybrid DD-ROM since the purely DD-ROM has not significantly improved the results in test case **a**.

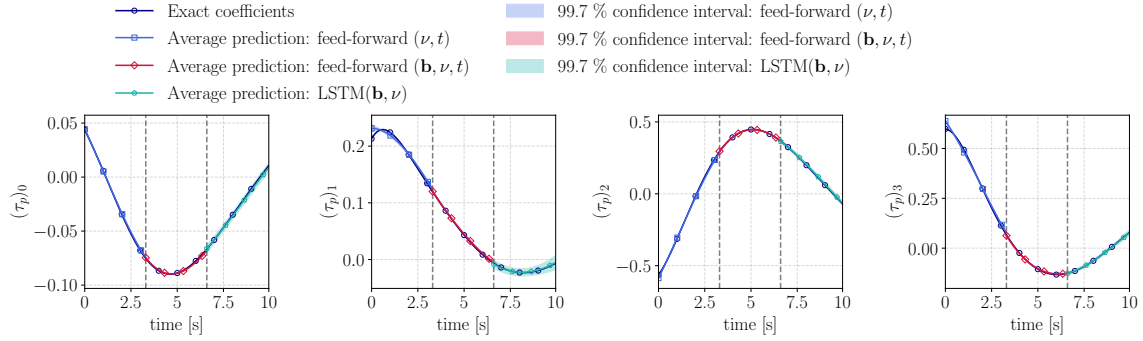


Figure 16: Correction terms' coefficients for $\nu = 5 \times 10^{-6} \text{ m}^2/\text{s}$ (in \mathcal{N}_{train}): neural networks predictions' average and POD projected exact coefficients.

Figures 17 and 18 show that the relative errors of the velocity and pressure fields w.r.t. the FOM, for two test viscosity values. Moreover, the value for Figure 17 is outside of the POD range.

The standard ROM approach completely blows up after a few time steps in both cases, because of the ill-conditioning of the system. In this case, the correction terms are necessary not only to improve the accuracy but also to ensure the stability of the reduced formulation.

On the one hand, in Figure 17 the viscosity value is the lowest taken into account, namely corresponding to the highest Reynolds number. In this case, the performance of all the DD-ROMs leads to a stabilized system with improved accuracy.

In both cases, the best performance is obtained with the multi-layer perceptron only having as input the system parameters, while the worst performance is the feed-forward which also considers as input the pressure coefficients. The average prediction obtained with the feed-forward(ν, t) network is similar to the one obtained by considering the exact coefficients, with higher confidence compared to the other neural networks. On the contrary to what was observed for test case **a.**, the cavity presents a monotone trend in time, which appears to be well captured through a mapping only depending on parameters (ν, t).

In conclusion, the hybrid DD-ROM approach may be used in reduced order systems both to improve the results and to avoid stability issues and ill-conditioning.

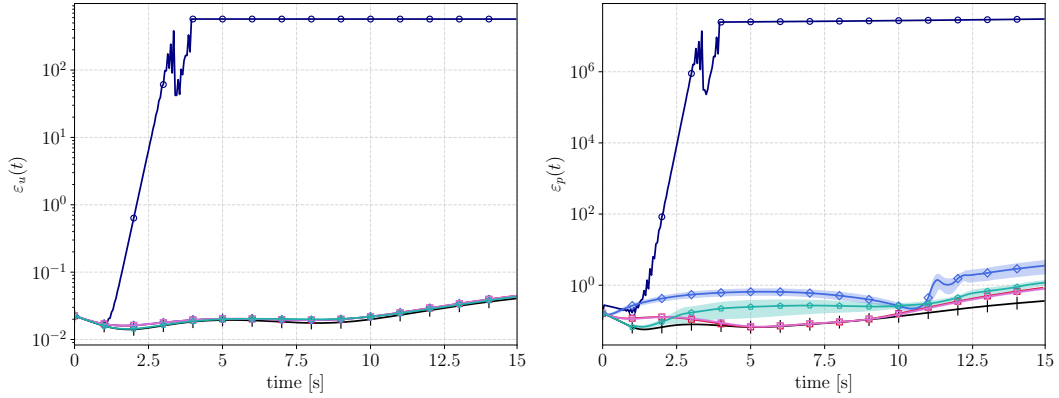
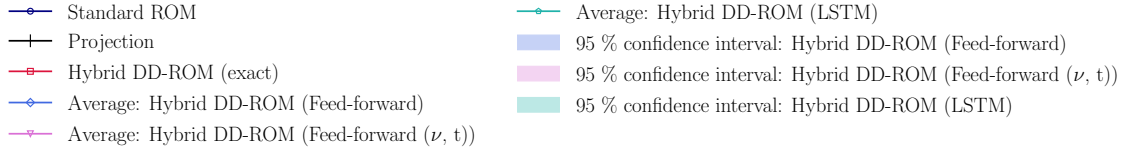
However, the method is still limited by the linearity of the POD, which is used to write system (18). Indeed, the correction terms added into the PPE-ROM system are obtained from the operators coming from a POD-Galerkin projection. Those operators in an advection-dominated test case and a marginally-resolved regime, may not well represent the dynamics of the system.

3.2.4 Graphical results

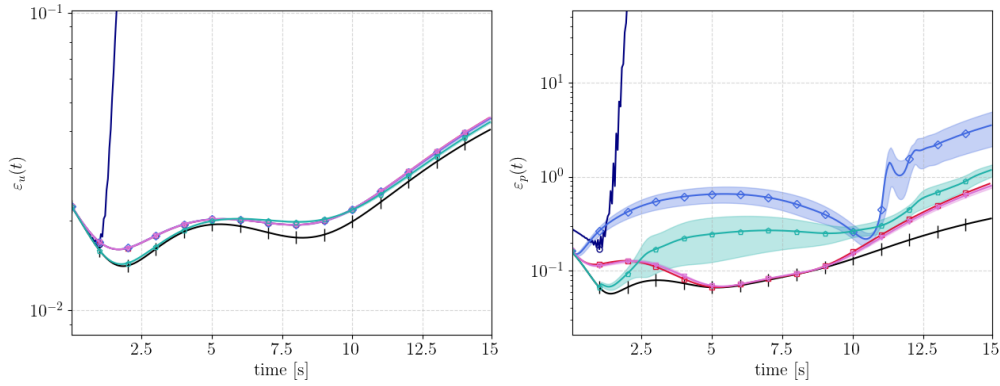
The graphical results for the velocity and pressure fields are represented in Figure 20 and 21, respectively. The results are for the final time instance of the online simulation, namely $t = 20 \text{ s}$.

We exclude the standard ROM from the graphical comparison since it blows up after a few time steps of the online ROM.

As already highlighted in the previous Subsection, Figures 20 and 21 show that the DD-ROM approximations are not as accurate as in the cylinder test case.



(a)



(b)

Figure 17: Relative errors for $\nu \in \mathcal{N}_{test}$, $\nu = 4 \times 10^{-6} \text{ m}^2/\text{s}$ for the pressure and the velocity magnitude fields, for the physics-based DD-ROMs, hybrid DD-ROMs, standard POD-Galerkin ROMs (first row). The second row represents a zoomed version of the error.

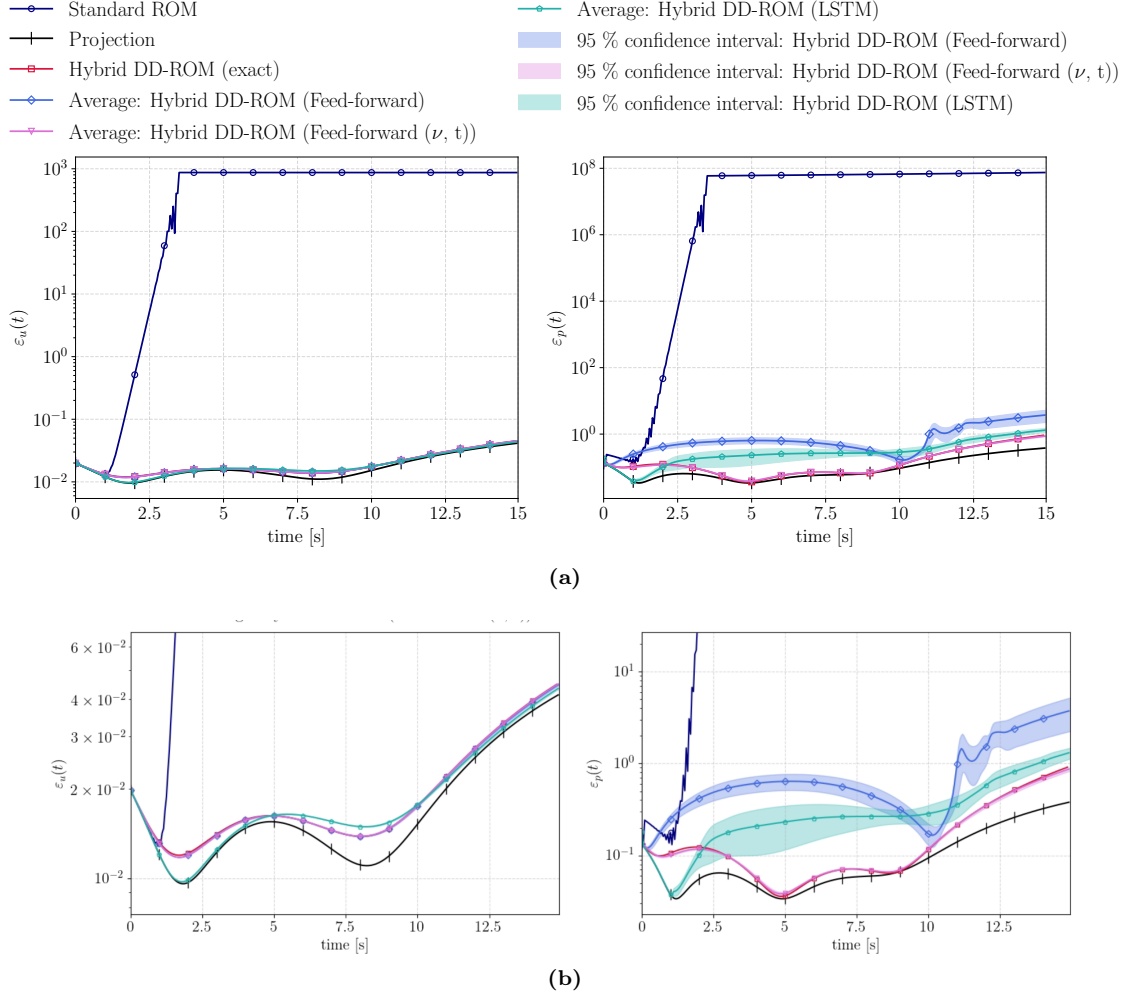


Figure 18: Relative errors for $\nu \in \mathcal{N}_{test}$, $\nu = 7 \times 10^{-6} \text{ m}^2/\text{s}$ for the pressure and the velocity magnitude fields, for the physics-based DD-ROMs, hybrid DD-ROMs, standard POD-Galerkin ROMs (first row). The second row represents a zoomed version of the error.

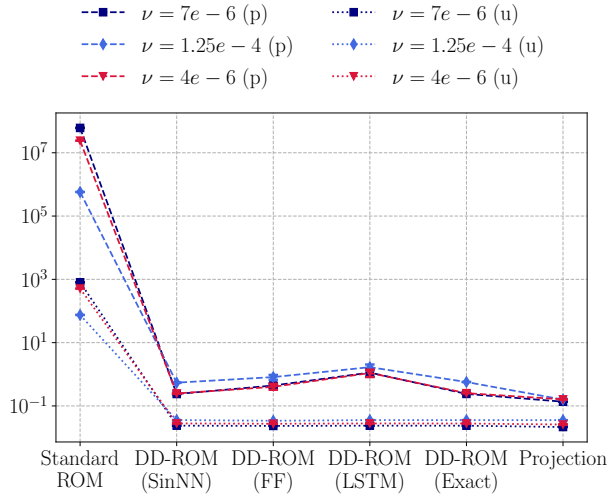


Figure 19: Integrals of relative errors over time for $\nu \in \mathcal{N}_{test}$ for the pressure and the velocity magnitude fields, in the standard ROM, hybrid DD-ROMs, and for the projection.

3.3. Discussion

This part of the manuscript is dedicated to a final comparison between the two test cases, for all the different ROMs proposed.

- **POD performance:** In general, as already pointed out, test case **b** is the most challenging. Indeed, the POD eigenvalues decay is smaller (Figures 4, 14) and the reconstruction errors are much higher, as can be seen for instance from the time integrals of the projection errors in Figures 10 and 19.
- **Standard ROM:** On the one hand, the standard ROM leads to relative errors increasing in time in the cylinder test case, as shown in Figure 9. On the other hand, in the cavity test case, the standard POD-Galerkin approach blows up after a few time steps. In this case, the POD-based operators may lead to a ill-conditioned reduced system.
- **Purely DD-ROM:** We only evaluate the performance of this model in test case **a** and the results slightly improve the standard ROM accuracy. Indeed, if we compare Figures 8 (with the purely DD-ROM results) and 9 (with the hybrid DD-ROM results), we notice that the effect of the correction terms acts in a more massive way on the system if combined with the physics-based DD-ROM. This aspect is deeply analysed in the non-parametric case in [21], where the authors showed that the combination of the data-driven methods provides always better results than the individual approaches. This is the reason why we decide to focus only on the hybrid approach in test case **b**.
- **Hybrid DD-ROM:**

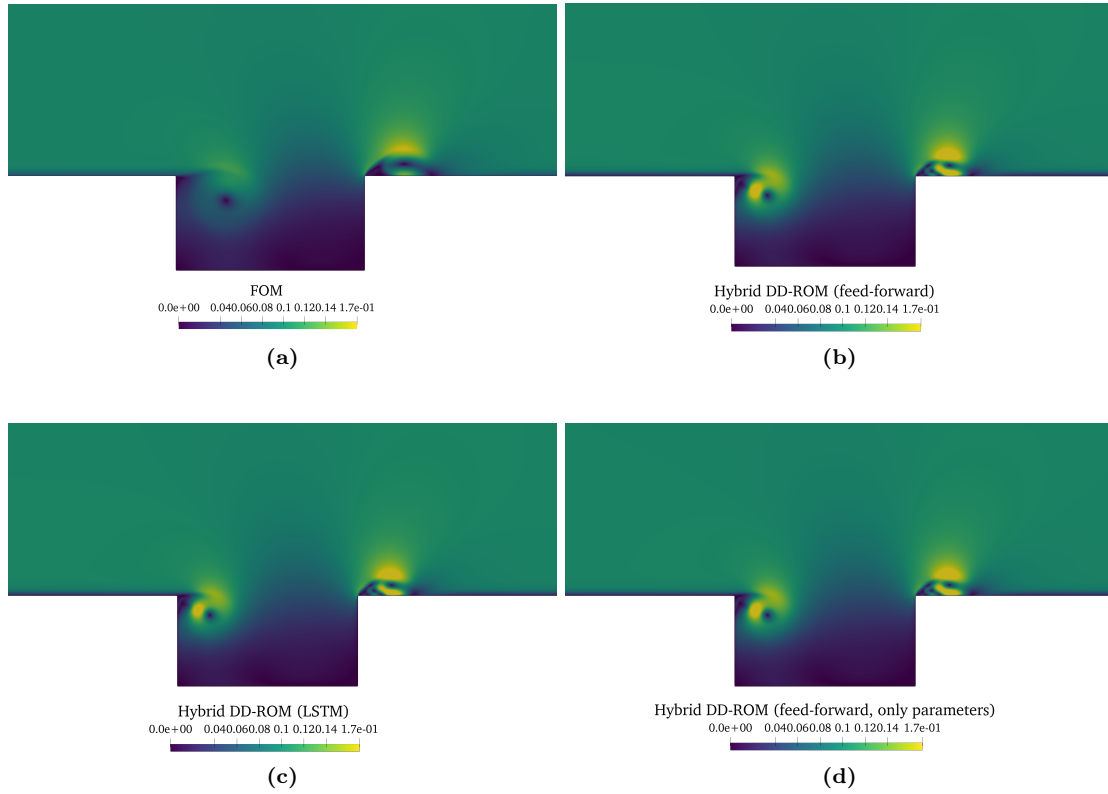


Figure 20: *Velocity magnitude fields at final instant of ROM. The standard ROM results are not represented here because the standard simulation blows up.*

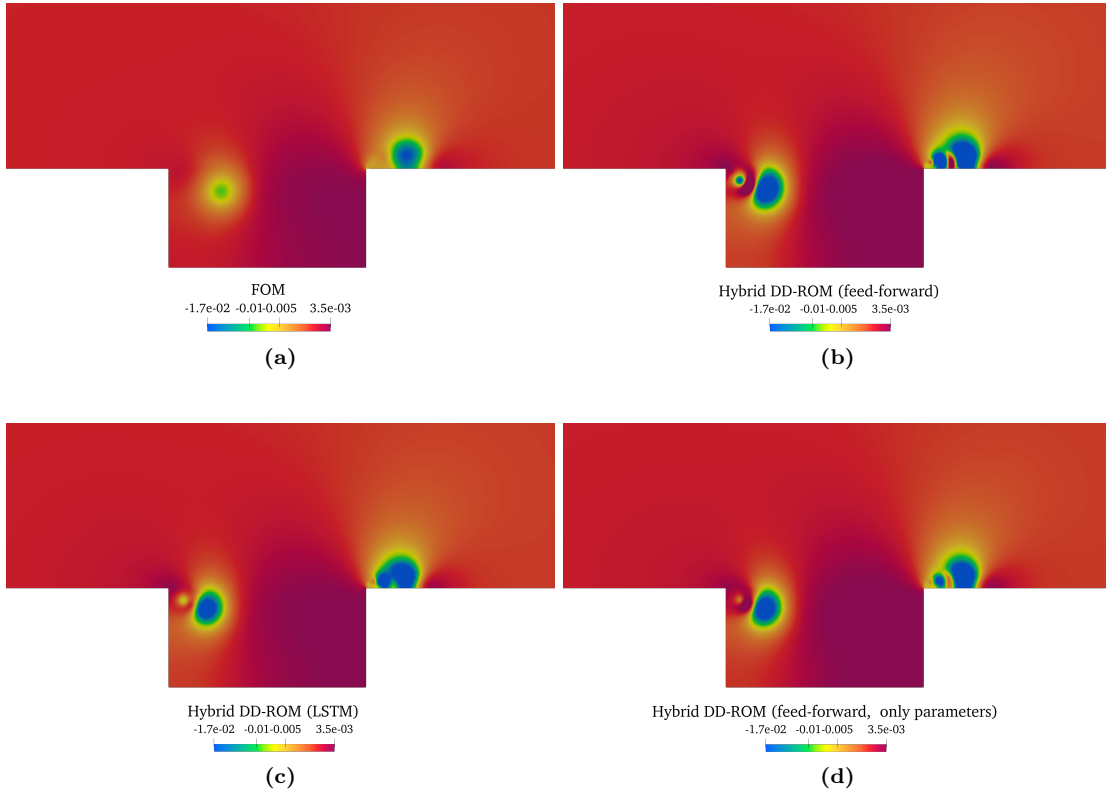


Figure 21: Pressure fields at final instant of ROM. The standard ROM results are not represented here because the standard simulation blows up.

- As a general consideration, the main difference among the two test cases, is that the DD-ROM acts as a *results-enhancer* for the cylinder, but also as a *system stabilizer* for the cavity case.
- In the first test case, the LSTM is the best-suited architecture to capture the dynamics of the correction terms. This can be explained with the fact that the LSTM inputs and outputs, namely the velocity/pressure coefficients and the correction coefficients, have the same periodic behavior. Considering a time-memory of about half-period, the network is also well performing in time extrapolation. However, when we consider the cavity test case, the best-suitable architecture is the multi-layer perceptron not depending on the pressure coefficients. This is because the pressure coefficients and the correction coefficients have a different behaviour.
- It is important to highlight that all the neural networks taken into account in both the test cases have a good performance in a predictive setting (Figures 6, 16), but the performance varies when the input coefficients are not anymore the *optimal* ones, namely the projected reduced coefficients. When the inputs are the coefficients \mathbf{a} and/or \mathbf{b} coming from the resolution of the dynamical system (5), the accuracy of the prediction is quite different and depends on the intrinsic relations between inputs and outputs.

4. CONCLUSIONS AND OUTLOOK

The project presented in this paper aims to enhance the classical ROM approaches using machine learning tools. The general paradigm of DD-ROMs was already presented in [21], but it is here extended to a more general parametric setup.

Section 1 introduces the problem and the issues of standard ROMs in capturing the evolution of the system’s dynamics.

Section 2 is dedicated to the presentation of the methodologies used in this work. In particular, we introduce the FOM used to collect the snapshots in 2.1, the POD-Galerkin ROM approach in 2.2, and the machine-learning enhanced ROMs in 2.3. In the last-mentioned part, we consider two types of enhancement: the *physics-based* DD-ROM, aimed to re-introduce the turbulence modeling at the ROM level, is briefly recalled in Subsection 2.3.1, whereas the *purely* DD-ROM, aimed to close the system through the modeling of the neglected modes, is presented in Subsection 2.3.2.

Finally, the numerical results are presented in Section 3, showing the effects of the machine-learning approaches on the periodic flow past a cylinder (3.1), and on the channel-driven cavity flow (3.2).

For each test case, we perform the offline stage in a parametric setting, considering as parameters time and the Reynolds number. After that, a POD eigenvalues analysis is performed (in 3.1.1 and 3.2.3), after which we focus our study on the *marginally-resolved* regime. In this framework, standard ROMs produce poor results and do not provide accurate reconstructions of the solutions.

For each test case, we investigate the effects of the machine learning approaches on the reduced dynamical system. In particular, we compared the results of three different types of neural network architectures in both test cases, spacing among LSTM architectures, *ad-hoc* architectures, and more classical multi-layer perceptron structures.

The results are presented in terms of: (i) neural networks performance directly in a predictive

setting (in 3.1.2 and 3.2.2); (ii) velocity and pressure relative errors with respect to the FOM counterpart for unseen configurations (in 3.1.3 and 3.2.3); (iii) graphical views of the fields at the ROM final time instance.

The final Subsection 3.3 makes a comparison between the two test cases in terms of performances.

In conclusion, we were able to provide in this work an algorithm able to enhance the POD-Galerkin results, acting also as a stabilizer in highly unsteady setups.

As pointed out for the cavity test case, the results' accuracy is influenced by the linearity of the POD approach. Hence, the method may be further improved introducing *nonlinearity* in the projection step, by replacing the POD with more advanced techniques, like autoencoders. This will be the focus of the authors' future research work.

Another extension of interest may be to include an *a-posteriori learning* inside the neural networks used to predict the correction terms. This would increase the training computational time, but improving the final accuracy without affecting the online prediction time.

ACKNOWLEDGEMENTS

We acknowledge the support by the European Commission H2020 ARIA (Accurate ROMs for Industrial Applications, GA 872442) project, by MIUR (Italian Ministry for Education University and Research) and by the European Research Council Consolidator Grant Advanced Reduced Order Methods with Applications in Computational Fluid Dynamics-GA 681447, H2020-ERC COG 2015 AROMA-CFD. This work has been conducted within the research activities of the consortium iNEST (Interconnected North-East Innovation Ecosystem), Piano Nazionale di Ripresa e Resilienza (PNRR) – Missione 4 Componente 2, Investimento 1.5 – D.D. 1058 23/06/2022, ECS00000043, supported by the European Union's NextGenerationEU program. We also acknowledge the support by INdAM-GNCS: Istituto Nazionale di Alta Matematica — Gruppo Nazionale di Calcolo Scientifico.

Giovanni Stabile acknowledges the financial support under the National Recovery and Resilience Plan (NRRP), Mission 4, Component 2, Investment 1.1, Call for tender No. 1409 published on 14.9.2022 by the Italian Ministry of University and Research (MUR), funded by the European Union – NextGenerationEU– Project Title ROMEU – CUP P2022FEZS3 - Grant Assignment Decree No. 1379 adopted on 01/09/2023 by the Italian Ministry of Ministry of University and Research (MUR).

The main computations in this work were carried out by the usage of ITHACA-FV [1], an open-source library and an implementation in OpenFOAM [2] for reduced order modeling techniques. Its developers and contributors are acknowledged.

REFERENCES

- [1] *ITHACA-FV*|*mathLab innovating with mathematics* website. <https://mathlab.sissa.it/ithaca-fv>.
- [2] *OpenFOAM* website. <https://openfoam.org/>.
- [3] S. E. Ahmed, S. Pawar, O. San, A. Rasheed, T. Iliescu, and B. R. Noack. On closures for reduced order models—A spectrum of first-principle to machine-learned avenues. *Physics of Fluids*, 33(9), 2021.
- [4] I. Akhtar, A. H. Nayfeh, and C. J. Ribbens. On the stability and extension of reduced-order Galerkin models in incompressible flows: a numerical study of vortex shedding. *Theoretical and Computational Fluid Dynamics*, 23:213–237, 2009.
- [5] I. Akhtar, Z. Wang, J. Borggaard, and T. Iliescu. A new closure strategy for proper orthogonal decomposition reduced-order models. 2012.
- [6] S. Ali, F. Ballarin, and G. Rozza. Stabilized reduced basis methods for parametrized steady Stokes and Navier–Stokes equations. *Computers & Mathematics with Applications*, 80(11):2399–2416, 2020.
- [7] M. Azaïez, T. C. Rebollo, and S. Rubino. Streamline derivative projection-based POD-ROM for convection-dominated flows. Part I: Numerical Analysis. *arXiv preprint <http://arxiv.org/abs/1711.09780>*, 2017.
- [8] F. Ballarin, A. Manzoni, A. Quarteroni, and G. Rozza. Supremizer stabilization of POD–Galerkin approximation of parametrized steady incompressible Navier–Stokes equations. *International Journal for Numerical Methods in Engineering*, 102(5):1136–1161, 2015.
- [9] P. Benner, S. Grivet-Talocia, A. Quarteroni, G. Rozza, W. Schilders, and L. Miguel Silveira. Model Order Reduction: Basic Concepts and Notation. In *Model Order Reduction: Volume 1: System-and Data-Driven Methods and Algorithms*, pages 1–14. De Gruyter, 2021.
- [10] P. Benner, W. Schilders, S. Grivet-Talocia, A. Quarteroni, G. Rozza, and L. Miguel Silveira. *Model Order Reduction: Volume 2: Snapshot-Based Methods and Algorithms*. De Gruyter, 2020.
- [11] P. Benner, W. Schilders, S. Grivet-Talocia, A. Quarteroni, G. Rozza, and L. Miguel Silveira. *Model order reduction: Volume 3: applications*. De Gruyter, 2020.
- [12] M. Bergmann, C. H. Bruneau, and A. Iollo. Enablers for robust POD models. *J. Comput. Phys.*, 228(2):516–538, 2009.
- [13] A. Chatterjee. An introduction to the Proper Orthogonal Decomposition. *Current science*, pages 808–817, 2000.
- [14] Z. Dar, J. Baiges, and R. Codina. Artificial neural network based correction for reduced order models in computational fluid mechanics. *Computer Methods in Applied Mechanics and Engineering*, 415:116232, 2023.

- [15] M. Girfoglio, A. Quaini, and G. Rozza. A hybrid projection/data-driven reduced order model for the navier-stokes equations with nonlinear filtering stabilization. *Journal of Computational Physics*, 486:112127, 2023.
- [16] G. Golub and W. Kahan. Calculating the singular values and pseudo-inverse of a matrix. *Journal of the Society for Industrial and Applied Mathematics, Series B: Numerical Analysis*, 2(2):205–224, 1965.
- [17] G. H. Golub and C. Reinsch. Singular value decomposition and least squares solutions. *Linear algebra*, 2:134–151, 1971.
- [18] M. Gunzburger, T. Iliescu, M. Mohebujjaman, and M. Schneier. An evolve-filter-relax stabilized reduced order stochastic collocation method for the time-dependent navier-stokes equations. *SIAM/ASA Journal on Uncertainty Quantification*, 7(4):1162–1184, 2019.
- [19] S. Hijazi, G. Stabile, A. Mola, and G. Rozza. Data-driven pod-galerkin reduced order model for turbulent flows. *Journal of Computational Physics*, 416:109513, 2020.
- [20] A. Iollo, S. Lanteri, and J. A. Désidéri. Stability properties of POD–Galerkin approximations for the compressible Navier–Stokes equations. *Theoret. Comput. Fluid Dyn.*, 13(6):377–396, 2000.
- [21] A. Ivagnes, G. Stabile, A. Mola, T. Iliescu, and G. Rozza. Hybrid data-driven closure strategies for reduced order modeling. *Applied Mathematics and Computation*, 448:127920, 2023.
- [22] A. Ivagnes, G. Stabile, A. Mola, T. Iliescu, and G. Rozza. Pressure data-driven variational multiscale reduced order models. *Journal of Computational Physics*, 476:111904, 2023.
- [23] A. Ivagnes, N. Tonicello, P. Cinnella, and G. Rozza. Enhancing non-intrusive reduced order models with space-dependent aggregation methods. *arXiv preprint arXiv:2403.05710*, 2024.
- [24] H. Jasak. Error analysis and estimation for the finite volume method with applications to fluid flows. 1996.
- [25] D. Kosambi. Statistics in function space. *DD Kosambi: Selected Works in Mathematics and Statistics*, pages 115–123, 2016.
- [26] K. Kunisch and S. Volkwein. Galerkin proper orthogonal decomposition methods for a general equation in fluid dynamics. *SIAM Journal on Numerical analysis*, 40(2):492–515, 2002.
- [27] C. L. Lawson and R. J. Hanson. *Solving least squares problems*. SIAM, Philadelphia, PA, 1995.
- [28] D. Lazzaro and L. B. Montefusco. Radial basis functions for the multivariate interpolation of large scattered data sets. *Journal of Computational and Applied Mathematics*, 140(1-2):521–536, 2002.
- [29] F. R. Menter. Two-equation eddy-viscosity turbulence models for engineering applications. *AIAA journal*, 32(8):1598–1605, 1994.

- [30] C. A. Micchelli. Interpolation of scattered data: distance matrices and conditionally positive definite functions. *Constructive approximation*, 2(1):11–22, 1986.
- [31] M. Mohebujjaman, L. Rebholz, and T. Iliescu. Physically-constrained data-driven, filtered reduced order modeling of fluid flows. *arXiv preprint arXiv:1806.00350*, 2018.
- [32] M. Mohebujjaman, L. G. Rebholz, and T. Iliescu. Physically constrained data-driven correction for reduced-order modeling of fluid flows. *International Journal for Numerical Methods in Fluids*, 89(3):103–122, 2019.
- [33] C. Mou, B. Koc, O. San, L. G. Rebholz, and T. Iliescu. Data-driven variational multiscale reduced order models. *Computer Methods in Applied Mechanics and Engineering*, 373:113470, 2021.
- [34] F. Moukalled, L. Mangani, M. Darwish, et al. *The finite volume method in computational fluid dynamics*, volume 113. Springer, 2016.
- [35] B. R. Noack and H. Eckelmann. A low-dimensional galerkin method for the three-dimensional flow around a circular cylinder. *Physics of Fluids*, 6(1):124–143, 1994.
- [36] B. R. Noack, P. Papas, and P. A. Monkewitz. The need for a pressure-term representation in empirical Galerkin models of incompressible shear flows. *Journal of Fluid Mechanics*, 523:339–365, 2005.
- [37] D. Papapicco, N. Demo, M. Girfoglio, G. Stabile, and G. Rozza. The neural network shifted-proper orthogonal decomposition: a machine learning approach for non-linear reduction of hyperbolic equations. *Computer Methods in Applied Mechanics and Engineering*, 392:114687, 2022.
- [38] K. Pearson. LIII. On lines and planes of closest fit to systems of points in space. *The London, Edinburgh, and Dublin philosophical magazine and journal of science*, 2(11):559–572, 1901.
- [39] F. Pichi, F. Ballarin, G. Rozza, and J. S. Hesthaven. An artificial neural network approach to bifurcating phenomena in computational fluid dynamics. *Computers & Fluids*, 254:105813, 2023.
- [40] O. Reynolds. IV. On the dynamical theory of incompressible viscous fluids and the determination of the criterion. *Philosophical transactions of the royal society of London*, (186):123–164, 1895.
- [41] C. W. Rowley, T. Colonius, and R. M. Murray. Model reduction for compressible flows using POD and Galerkin projection. *Phys. D*, 189(1):115–129, 2004.
- [42] G. Rozza, D. Huynh, and A. Manzoni. Reduced basis approximation and a posteriori error estimation for Stokes flows in parametrized geometries: roles of the inf-sup stability constants. *Numerische Mathematik*, 125(1):115–152, 2013.
- [43] G. Rozza, D. B. P. Huynh, and A. T. Patera. Reduced basis approximation and a posteriori error estimation for affinely parametrized elliptic coercive partial differential equations. *Arch. Comput. Method. E.*, 15(3):229–275, 2008.

- [44] G. Rozza, G. Stabile, and F. Ballarin. *Advanced Reduced Order Methods and Applications in Computational Fluid Dynamics*. Society for Industrial & Applied Mathematics, 2022.
- [45] G. Rozza and K. Veroy. On the stability of the reduced basis method for Stokes equations in parametrized domains. *Comput. Methods Appl. Mech. Engrg.*, 196(7):1244–1260, 2007.
- [46] F. Salmoiraghi, A. Scardigli, H. Telib, and G. Rozza. Free-form deformation, mesh morphing and reduced-order methods: enablers for efficient aerodynamic shape optimisation. *International Journal of Computational Fluid Dynamics*, 32(4-5):233–247, 2018.
- [47] O. San and T. Iliescu. Proper orthogonal decomposition closure models for fluid flows: Burgers equation. *arXiv preprint arXiv:1308.3276*, 2013.
- [48] G. Stabile, S. Hijazi, A. Mola, S. Lorenzi, and G. Rozza. POD-Galerkin reduced order methods for CFD using Finite Volume Discretisation: vortex shedding around a circular cylinder. *Communications in Applied and Industrial Mathematics*, 8(1):210–236, 2017.
- [49] G. Stabile and G. Rozza. Finite volume POD-Galerkin stabilised reduced order methods for the parametrised incompressible Navier–Stokes equations. *Computers & Fluids*, 173:273–284, 2018.
- [50] S. K. Star, G. Stabile, F. Belloni, G. Rozza, and J. Degroote. A novel iterative penalty method to enforce boundary conditions in Finite Volume POD-Galerkin reduced order models for fluid dynamics problems. *Communications in Computational Physics*, 30(1):34–66, 2021.
- [51] M. Strazzullo, F. Ballarin, T. Iliescu, and C. Canuto. New feedback control and adaptive evolve-filter-relax regularization for the navier-stokes equations in the convection-dominated regime. *arXiv preprint arXiv:2307.00675*, 2023.
- [52] M. Strazzullo, M. Girfoglio, F. Ballarin, T. Iliescu, and G. Rozza. Consistency of the full and reduced order models for evolve-filter-relax regularization of convection-dominated, marginally-resolved flows. *International Journal for Numerical Methods in Engineering*, 123(14):3148–3178, 2022.
- [53] S. Walton, O. Hassan, and K. Morgan. Reduced order modelling for unsteady fluid flow using proper orthogonal decomposition and radial basis functions. *Applied Mathematical Modelling*, 37(20-21):8930–8945, 2013.
- [54] Y. Wang, B. Yu, Z. Cao, W. Zou, and G. Yu. A comparative study of POD interpolation and POD projection methods for fast and accurate prediction of heat transfer problems. *International Journal of Heat and Mass Transfer*, 55(17-18):4827–4836, 2012.
- [55] S. Wold, K. Esbensen, and P. Geladi. Principal component analysis. *Chemometrics and intelligent laboratory systems*, 2(1-3):37–52, 1987.
- [56] X. Xie, M. Mohebujjaman, L. G. Rebholz, and T. Iliescu. Data-driven filtered reduced order modeling of fluid flows. *SIAM Journal on Scientific Computing*, 40(3):B834–B857, 2018.
- [57] X. Xie, C. Webster, and T. Iliescu. Closure learning for nonlinear model reduction using deep residual neural network. *Fluids*, 5(1):39, 2020.

- [58] M. Zancanaro, M. Mrosek, G. Stabile, C. Othmer, and G. Rozza. Hybrid neural network reduced order modelling for turbulent flows with geometric parameters. *Fluids*, 6(8):296, 2021.

A. NEURAL NETWORKS HYPERPARAMETERS

In this Section we specify the hyperparameters of the machine learning techniques used in this work.

A.1. Neural networks’ architecture for the hybrid DD-ROM in test case **a**

This Section is dedicated to the structure of the neural networks considered in test case **a** to model the mappings \mathcal{G} (used to compute the eddy-viscosity coefficients), and \mathcal{M} (used to compute the correction coefficients).

Table 2 shows the hyperparameters’ settings for the different cases considered. In the Table we reported the structure of the hidden layers as a list of numbers, where the length of the list indicates the number of hidden layers and the values in the list indicate the number of neurons for each layer. In all the models proposed, the final layer is composed of only linear operations. In particular, for the LSTM network, we considered a sequence length, N_{seq} in the Table, which is $N_{\text{seq}} \sim T/2$, where T is the flow period.

Moreover, for what concerns the SinNN architecture, the values N_1 and N_2 in 22 have the aim of amplifying the frequency of the periodic expressions proposed, while n is the number of sinusoids considered in the final combination. In our case, $N_1 = 50$, $N_2 = 1000$, and $n = 20$.

Moreover, in every mapping we consider a regularization in the loss, namely an additional term \mathcal{L}_{add} depending on the weights’ L^2 norm. The additional term is expressed as:

$$\mathcal{L}_{\text{add}} = \omega \|\boldsymbol{\theta}\|_{L^2}^2, \quad (21)$$

where $\boldsymbol{\theta}$ includes all the weights of the neural network, and $\omega = 1 \times 10^{-6}$ in our setting.

The optimization employs the Adam algorithm in all the networks.

Table 2: *Neural networks setting for test case **a**.*

<i>Mapping</i>	<i>Network</i>	<i>Hidden layers</i>	<i>Non-linearity</i>	<i>Learning rate</i>	<i>Stopping epoch</i>
$\mathbf{g} = \mathcal{G}(\mathbf{a}, \nu, t)$	Feed-forward	[20, 20, 20]	Softplus	1×10^{-3}	10000
$\boldsymbol{\tau} = \mathcal{M}(\mathbf{a}, \mathbf{b}, \nu, t)$	Feed-forward	[20, 20, 20]	ReLU	1×10^{-3}	6000
$\boldsymbol{\tau} = \mathcal{M}(\mathbf{a}, \mathbf{b}, \nu)$	LSTM	[20, 20], $N_{\text{seq}}:100$	X	1×10^{-3}	6000
$\mathbf{p} = \text{NN}_1(\nu)$	Feed-forward	[5, 5]	Leaky ReLU	1×10^{-3}	6000
$\boldsymbol{\tau} = \text{NN}_2(\mathbf{o})$	Feed-forward	[20, 20]	Leaky ReLU		

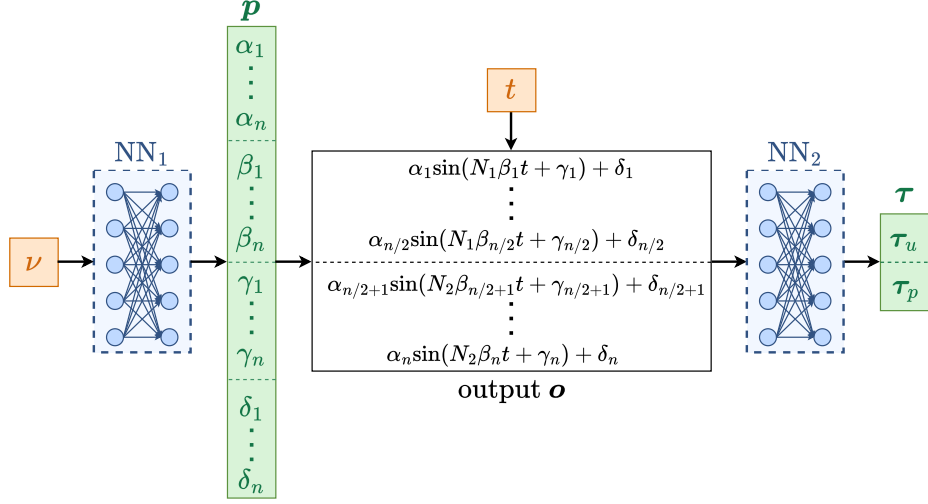


Figure 22: Schematic architecture of the SinNN neural network considered to find the correction coefficients in test case **a**. The orange boxes are the inputs needed to train the SinNN as a function of the parameters only, namely $\mathcal{M}(\nu, t)$. NN_1 and NN_2 are two feed-forward fully connected neural networks embedded in the proposed structure and described in Table 2.

A.2. Neural networks' architecture for the hybrid DD-ROM in test case **b**

This Section is dedicated to the specification of the hyperparameters in test case **b**. In particular, Table 3 reports the specifics of all the architectures proposed. Also in this case, we apply a weight regularization, considering the same expression in (21), and with the same weight decay $\omega = 1 \times 10^{-6}$. Moreover, as can be seen from Table 3, the learning rate is decreased with a rate of 1/5 every 3000 epochs, in order to avoid picks of the loss during the training process.

We remark that in LSTM networks in both Tables 2 and 3, no activation function is considered. The optimization employs the Adam algorithm, as in test case **a**.

Table 3: *Neural networks setting for test case b. In the learning rate of the mapping \mathcal{M} , we call t_{epoch} the current epoch, $N_{step} = 3000$ the epochs' interval to decrease the learning rate, $\gamma = 0.2$ the corresponding decreasing rate.*

<i>Mapping</i>	<i>Network</i>	<i>Hidden layers</i>	<i>Non-linearity</i>	<i>Learning rate</i>	<i>Stopping epoch</i>
$\mathbf{g} = \mathcal{G}(\mathbf{a}, \nu, t)$	Standard feed-forward	[20, 20, 20]	Softplus	1×10^{-3}	10000
$\tau_p = \mathcal{M}(\mathbf{b}, \nu, t)$	Feed-forward	[20, 20, 20]	Softplus	$(1 \times 10^{-3})\gamma^{\lfloor \frac{t_{epoch}}{N_{step}} \rfloor}$	10000
$\tau_p = \mathcal{M}(\mathbf{b}, \nu)$	LSTM	[20, 20], $N_{seq}:20$	X	$(1 \times 10^{-3})\gamma^{\lfloor \frac{t_{epoch}}{N_{step}} \rfloor}$	10000
$\tau_p = \mathcal{M}(\nu, t)$	Feed-forward	[5, 5]	Softplus	$(1 \times 10^{-3})\gamma^{\lfloor \frac{t_{epoch}}{N_{step}} \rfloor}$	10000